Dynamics of a Small Autonomous Underwater Vehicle That Tows a Large Payload

Michael E. Kepler

Thesis submitted to the Faculty of the

Virginia Polytechnic Institute and State University

in partial fulfillment of the requirements for the degree of

Master of Science

in

Electrical Engineering

Daniel J. Stilwell, Chair

Stefano Brizzolara

William T. Baumann

July 20, 2018

Blacksburg, Virginia

Keywords: Multi-body systems, Dynamics, Autonomous Underwater Vehicles, Rope Dynamics

Dynamics of a Small Autonomous Underwater Vehicle That Tows a Large Payload

Michael E. Kepler

(ABSTRACT)

This thesis presents the derivation of the dynamic model of an autonomous underwater vehicle that tows a large payload. Our analysis is motivated by the fact that the payload is so large that it cannot be modeled by simply appending its dynamics to the dynamics of the autonomous underwater vehicle. Hence, the coupling between the vehicle and payload must be fully modeled. Furthermore, several approximation techniques based on analytic and empirical formulations are investigated for computing the hydrodynamic coefficients of the vehicle. Efficacy and limitations of the approximation techniques are assessed by comparison with hydrodynamic coefficients that are estimated using high-fidelity computational fluid dynamics simulations.

Dynamics of a Small Autonomous Underwater Vehicle That Tows a Large Payload

Michael E. Kepler

(GENERAL AUDIENCE ABSTRACT)

This thesis presents the model to used to predict the motion of an autonomous underwater vehicle that tows a large object. Our analysis is motivated by the fact that the size of the object is so large that it will have a substantial impact on the motion of the vehicle, and likewise the vehicle will have a substantial impact on the object, requiring that the interaction between the two bodies to be fully modeled. The fluid forces and moments acting on the vehicle are approximated using techniques from hydrodynamic theory and experimental results. The accuracy of the approximation is assessed by comparing of the estimated forces and moments with those seen in high-fidelity simulations.

Acknowledgments

I would like to express my gratitude to my brother Ray and my sister-in-law Gladys for the sacrifices their family has made that allowed me to leave home and pursue graduate studies at Virginia Tech. I would like to thank my mother, Theresa, for the constant love and support she has shown me throughout my entire life. I would not be in the position of success that I am today without all the sacrifices she has made. I would like to thank all my fellow colleagues in the ASCL lab for all the help and support they have provided. In particular I would like to thank Stephen Krauss for his help conducting rope field trials, Scott Gibson for his dynamics and controls insight that aided me throughout my entire master's program, Jorge Jimenez for his contributions to the guidance system and internal electronics of the SATLP vehicle, and lastly Suraj Pawar who was responsible for the mechanical design of the SATLP vehicle, and performed CFD simulations that a large portion of this thesis was dependent on. I would like to extend my gratitude to Dr. Craig Woolsey, who on more than one occasion met with me and provided helpful insight into several aspects regarding multi-body dynamics and control. I would like to thank Dr. Stefano Brizzolara and Dr. Wayne Neu for their oversight and guidance provided in regards to the hydrodynamic work presented in this thesis. Lastly, but most importantly I would like to thank my advisor Dr. Daniel Stilwell for giving me this research opportunity and for his help and guidance with all aspects of this thesis.

Contents

List of Figures

List of Tables

List of Abbreviations

AHRS Attitude and heading reference system

ASE Analytical and Semi-empirical

AUV Autonomus underwater vehicle

CAD Computer aided design

CB Center of buoyancy

CFD Computational fluid dynamics

CG Center of gravity

DOF Degree of freedom

LHS Left hand side

NDRE Norwegian Defense Research Establishment

NPS Naval Postgraduate School

PID Proportional integral derivative

PMM Planar Motion Mechanism

RHS Right hand side

SATLP Small AUV Towing a Large Payload

SMC Sliding mode control

VPMM Virtual Planar Motion Mechanism

Chapter 1

Introduction

The Small Autonomous Underwater Vehicle Tows a Large Payload (SATLP) vehicle has been developed to tow a payload whose drag is many times larger than that of the vehicle. The payload trajectory is to be precisely controlled so that the payload arrives at a desired location with a desired horizontal orientation at a desired time. The forces and moments induced from the payload drag are seen as restorative in nature, such that as the vehicle tries to turn, the rope generates a counter force and moment to straighten the vehicle, limiting the turning maneuverability of the vehicle.

Conventional autonomous underwater vehicles (AUV) are controlled using control surfaces located at the aft end of the vehicle. In an effort to generate a greater turning moment for the vehicle, placement of control surfaces at the nose of the vehicle is evaluated.

To evaluate how fin placement affects the dynamic behavior of the vehicle, we investigate the use of analytic and semi-empirical (ASE) methods for computing coefficients in hydrodynamic models. To assess the utility of the coefficients, the high fidelity forces and moments for a prescribed motion seen in computational fluid dynamics (CFD) simulations are compared to those predicted by the ASE coefficients for the same prescribed motion.

The payload considered for this study is a heavy-gauge rope. The rope is modeled by N discrete lumped spherical masses, connected by massless links treated as spring-damper elements. Since the lumped masses are treated as spheres, solely translational motion is

experienced by each mass.

Traditional marine tow systems employ a vessel, whose mass is orders of magnitude greater than the towed payload. Consequently, the towed payload forces acting on the vessel are considered negligible and not modeled. Such an assumption becomes invalid when the vessel is replaced by an underwater vehicle, whose mass is no longer orders of magnitude greater than the payload. Therefore, the dynamical model must capture the effects of coupling between the vehicle and payload.

Chapter 5 presents a proportional feedback control system for the steering autopilot. Motion of the system is constrained to the horizontal plane. The performance of the closed-loop system is assessed by numerical simulation.

Chapter 2

Vehicle Model

This chapter presents the equations of motion for the vehicle, consisting of the kinematic relations used to express the local vehicle velocities in the inertial frame, and the vehicle dynamics governed by the external forces and moments acting on the vehicle.

2.1 Vehicle Kinematics

To describe the motion of the vehicle, an inertial reference frame $\mathcal{F}_I$ and a vehicle-fixed reference frame $\mathcal{F}_V$ are defined. The origin of $\mathcal{F}_V$ is located at the center of buoyancy (CB), coincident with the geometric center of the vehicle such that the position of the CB is $\mathrm{p}_V^B = [0,\ 0,\ 0]^\mathsf{T}$. The subscript corresponds to the frame of reference, with V referring to the vehicle frame. Both reference frames follow right-hand convention. The pose of $\mathcal{F}_V$ relative to $\mathcal{F}_I$ is expressed

$$\eta = \begin{bmatrix} \eta_1^\mathsf{T}, & \eta_2^\mathsf{T} \end{bmatrix}^\mathsf{T} = \begin{bmatrix} x, & y, & z, & \phi, & \theta, & \psi \end{bmatrix}^\mathsf{T}, \tag{2.1}$$

where $\eta_1 = [x,\ y,\ z]^\mathsf{T}$ represents the vehicle's inertial position, and $\eta_2 = [\phi,\ \theta,\ \psi]^\mathsf{T}$ is the attitude of the vehicle represented using Euler angles, where ϕ, θ, and ψ are the roll, pitch, and yaw angles, respectively. The velocity of the vehicle expressed in the vehicle frame $\mathcal{F}_V$

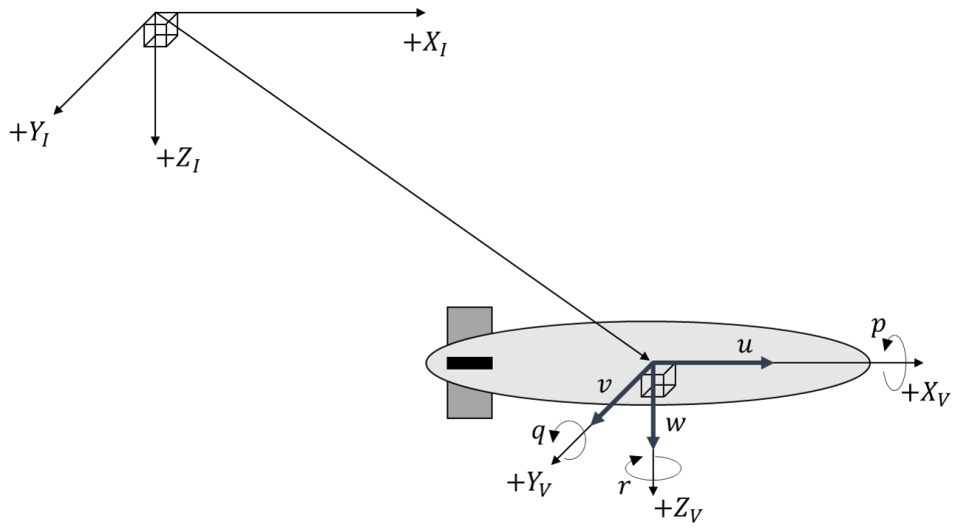

Figure 2.1: Inertial and vehicle reference frame along with the definitions of the translational and rotational velocities

is

$$\nu = \begin{bmatrix} \nu_1^\mathsf{T}, & \nu_2^\mathsf{T} \end{bmatrix}^\mathsf{T} = \begin{bmatrix} u, & v, & w, & p, & q, & r \end{bmatrix}^\mathsf{T}. \tag{2.2}$$

The translational velocities of the vehicle are denoted by $\nu_1 = [u,\ v,\ w]^\mathsf{T}$, where the surge, sway, and heave velocities are denoted by u, v, and w, respectively. The angular velocities of the vehicle are denoted by $\nu_2 = [p,\ q,\ r]^\mathsf{T}$, where p, q, and r are the angular rates about the principal axes of the vehicle X_V, Y_V, and Z_V, respectively. The local vehicle velocities are depicted in Figure 2.1.

The local translational velocities of the vehicle are expressed in the inertial frame by employing three principal rotations about the Z, Y, and X axes. This sequence of rotations is commonly referred to as a (ZYX) or (3-2-1) rotation. The transformation expressing the local translational velocities in the inertial frame is

$$\dot{\eta}_1 = R_{IV}^{\eta_1} \nu_1, \tag{2.3}$$

where the linear velocity transformation matrix is

$$R_{IV}^{\eta_1} = \begin{bmatrix} \cos(\psi)\cos(\theta) & -\sin(\psi)\cos(\phi) + \cos(\psi)\sin(\theta)\sin(\phi) & \sin(\psi)\sin(\phi) + \cos(\psi)\cos(\phi)\sin(\theta) \\ \sin(\psi)\cos(\theta) & \cos(\psi)\cos(\phi) + \sin(\phi)\sin(\theta)\sin(\psi) & -\cos(\psi)\sin(\phi) + \sin(\theta)\sin(\psi)\cos(\phi) \\ -\sin(\theta) & \cos(\theta)\sin(\phi) & \cos(\theta)\cos(\phi) \end{bmatrix}. \tag{2.4}$$

The Eular angle rate vector is related to the local angular velocity vector by the transformation

$$\dot{\eta}_2 = R_{IV}^{\eta_2} \nu_2, \tag{2.5}$$

where the angular velocity transformation matrix is

$$R_{IV}^{\eta_2} = \begin{bmatrix} 1 & \sin(\phi)\tan(\theta) & \cos(\phi)\tan(\theta) \\ 0 & \cos(\phi) & -\sin(\phi) \\ 0 & \frac{\sin(\phi)}{\cos(\theta)} & \frac{\cos(\phi)}{\cos(\theta)} \end{bmatrix}. \tag{2.6}$$

Augmenting the linear and angular velocity transformations into a single transformation matrix yields

$$R_{IV} = \begin{bmatrix} R_{IV}^{\eta_1} & 0_{3\times3} \\ 0_{3\times3} & R_{IV}^{\eta_2} \end{bmatrix}. \tag{2.7}$$

Thus the local vehicle velocities are expressed in the inertial frame using the transformation

$$\dot{\eta} = R_{IV} \nu. \tag{2.8}$$

To ensure that $R_{IV}^{\eta_2}$ is well defined, it is assumed that the pitch angle $\theta \neq \pm 90°$. This as-

sumption prohibits maneuvers in which the vehicle is pitched entirely nose up or down. This assumption is not restrictive since those motions are not of interest for the application at hand. For applications in which this assumption does not hold, alternative attitude representations can be achieved using quaternions. A detailed exposition of attitude representation using Euler angles and quaternions can be found in Chapter 2 of [9].

The subscript of R_{IV} is used to signify that this rotation matrix transforms coordinates expressed in $\mathcal{F}_V$ to coordinates expressed in $\mathcal{F}_I$. Conversely, the rotation matrix that transforms coordinates in $\mathcal{F}_I$ to $\mathcal{F}_V$ is denoted by

$$R_{VI} = R_{IV}^{-1} = \begin{bmatrix} (R_{IV}^{\eta_1})^{-1} & 0_{3\times 3} \\ 0_{3\times 3} & (R_{IV}^{\eta_2})^{-1} \end{bmatrix}, \tag{2.9}$$

where the matrix inverses are given by

$$(R_{IV}^{\eta_1})^{-1} = (R_{IV}^{\eta_1})^{\mathsf{T}}, \qquad (R_{IV}^{\eta_2})^{-1} = \begin{bmatrix} 1 & 0 & -\sin(\theta) \\ 0 & \cos(\phi) & \cos(\theta)\sin(\phi) \\ 0 & -\sin(\phi) & \cos(\theta)\cos(\phi) \end{bmatrix}. \tag{2.10}$$

2.2 Geometric Vehicle Profile

Derivation of the forces and moments acting on the vehicle requires a geometric description of the vehicle profile. For conventional streamline vehicles that are bodies of revolution, the shape is defined by specifying the radius $R(x)$ as a function of the axial position x along the longitudinal axis body, referenced from the origin of the vehicle.

A generic vehicle configuration consists of a hull and control fins. The radius of the fin is

specified by $R_f(x)$, which is presently treated as a constant such that

$$R_f(x) = h_f, \qquad \forall\ x \in [x_{f_1}, x_{f_2}], \tag{2.11}$$

with h_f denoting the height of the fin above the centerline of the vehicle. The axial position of the trailing and leading edge of the fin is denoted by x_{f_1} and x_{f_2}, respectively.

The prolate spheroid and the Myring profile [26] are two geometries that can be used to model the body of the vehicle. The prolate spheroid approximation is appealing because there exist closed-form analytic solutions to describe fluid forces and moments acting on the body. The Myring profile [26] is appealing because the shape is designed to minimize hydrodynamic drag for a vehicle. Thus designers for vehicles like the REMUS [28], and the MAYA [6] base the geometries of their vehicle off of the Myring profile.

The radius along the body of a prolate spheroid is given by

$$R_b(x) = \frac{d_v}{2}\sqrt{1 - \left(\frac{2x}{l_v}\right)^2}, \qquad x \in \left[x_{t1}, x_{n2}\right], \tag{2.12}$$

where the length and max diameter of the body are denoted by l_v and d_v, respectively. The aft end of tail section is specified by x_{t1}, and the bow end of the nose section by x_{n2}.

The Myring profile has three separate functions to specify the radius for the nose, midbody, and tail sections of the body, specifically

$$R_b(x) = \begin{cases} R_n(x) & x_{n_1} \le x \le x_{n_2} \\ R_m(x) & x_{m_1} \le x \le x_{m_2} \\ R_t(x) & x_{t_1} \le x \le x_{t_2} \end{cases}, \tag{2.13}$$

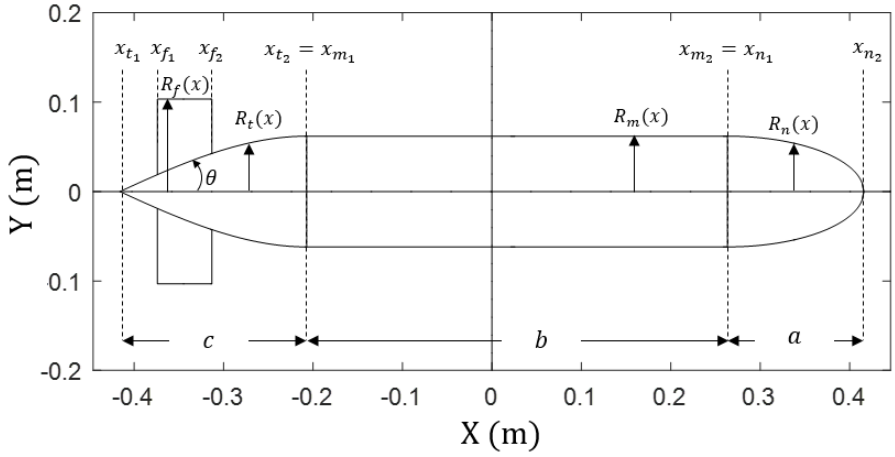

Figure 2.2: xy-projection of a tail finned Myring vehicle profile

where,

$$R_n(x) = \frac{1}{2}d_v\left[1 - \left(\frac{(x_{n_2} - x) - a}{a}\right)^2\right]^{\frac{1}{n}},$$

$$R_m(x) = \frac{1}{2}d_v,$$

$$R_t(x) = \frac{1}{2}d_v - \left(\frac{3d_v}{2c^2} - \frac{\tan\theta}{c}\right)\Big((x_{n_2} - x) - (a+b)\Big)^2 + \left(\frac{d_v}{c^3} - \frac{\tan\theta}{c^2}\right)\Big((x_{n_2} - x) - (a+b)\Big)^3.$$

The index of the nose shape is given by the parameter n. Figure 2.2 shows an xy-projection of the vehicle profile, illustrating the definitions of the Myring profile parameters. The control fins are arranged in a cruciform configuration, hence the xz-projection will mirror the xy-projection. A detailed discussion on the Myring vehicle profile and its parameters can be found in [26].

2.3 Six Degree of Freedom Vehicle Dynamics Model

The nonlinear dynamic model of the vehicle is expressed in matrix form as

$$M_V^{RB}\dot{\nu} + C_V^{RB}(\nu)\nu = \tau_V^A + \tau_V^D + \tau_V^G + \tau_V^C + \tau_V^R, \tag{2.14}$$

where the rigid body forces and moments experienced by the vehicle are on the left-hand side of the equation, and the sum of external forces and moments acting on the vehicle are on the right-hand side, consisting of forces due to added mass A, hydrodynamic damping D, restorative forces G, control inputs C, and the rope R. The subscript V denotes the vehicle-fixed reference frame. The forces and moments are presented with respect to the local vehicle frame. Therefore for the remainder of this chapter, unless explicitly specified, subscripts are not used to specify the frame of reference, except for the terms introduced in (2.14).

2.3.1 Rigid Body Forces and Moments

The rigid body forces and moments experienced by the vehicle can be derived using Euler's first and second axioms based on the conservation of linear and angular momentum. An expression for the complete rigid body forces and moments is

$$\tau_V^{RB} = M_V^{RB}\dot{\nu} + C_V^{RB}(\nu)\nu. \tag{2.15}$$

A derivation of the rigid body expressions (2.15) can be found in Chapter 2 of [8]. In practice, vehicles are often ballasted such that the center of gravity (CG), relative to the vehicle origin is $r_V^G = [0,\ 0,\ z_G]^\mathsf{T}$, where having $z_G > 0$ is desirable for roll stability of the vehicle. Furthermore, since the vehicle origin is located at the geometric center of the vehicle, and

the vehicle possesses top/bottom and port/starboard symmetry, the off-diagonal elements of the inertia tensor J are negligible, thus $J \approx \text{diag}\{J_x, J_y, J_z\}$ [8, Ch. 2]. For $r_V^G = [0,\ 0,\ z_G]^\mathsf{T}$, and $J \approx \text{diag}\{J_x, J_y, J_z\}$, the rigid body mass matrix is expressed as

$$M_V^{RB} = \begin{bmatrix} m_v & 0 & 0 & 0 & m_v z_G & 0 \\ 0 & m_v & 0 & -m_v z_G & 0 & 0 \\ 0 & 0 & m_v & 0 & 0 & 0 \\ 0 & -m_v z_G & 0 & J_x & 0 & 0 \\ m_v z_G & 0 & 0 & 0 & J_y & 0 \\ 0 & 0 & 0 & 0 & 0 & J_z \end{bmatrix}, \tag{2.16}$$

where m_v denotes the dry mass of the vehicle. Defining motion relative to a rotating reference frame introduces Coriolis and centrifugal forces. The Coriolis matrix is

$$C_V^{RB}(\nu) = \begin{bmatrix} 0 & 0 & 0 & m_v z_G r & m_v w & -m_v v \\ 0 & 0 & 0 & -m_v w & m_v z_G r & m_v u \\ 0 & 0 & 0 & -m_v(z_G p - v) & -m_v(z_G q + u) & 0 \\ -m_v z_G r & m_v w & m_v(z_G p - v) & 0 & J_z r & -J_y q \\ -m_v w & -m_v z_G r & m_v(z_G q + u) & -J_z r & 0 & J_x p \\ m_v v & -m_v u & 0 & J_y q & -J_x p & 0 \end{bmatrix}. \tag{2.17}$$

Computer aided design (CAD) software packages compute the dry mass of the vehicle m_v and the inertia tensor J. However, if a CAD model is not readily available, the inertia tensor can be computed by approximating the vehicle as a cylinder [2]. For a cylinder of length L

and radius r, the moments of inertia are

$$J_x = \frac{1}{2} m_v \mathrm{r}^2, \qquad J_y = J_z = \frac{1}{12} m_v (3\mathrm{r}^2 + L^2), \tag{2.18}$$

where the subscript of J specifies the axis of rotation.

2.3.2 Forces and Moments Due to Added Mass

For a body to accelerate through a fluid that would otherwise be at rest, it must impart kinetic energy to the surrounding fluid, such that as the body passes through, the fluid moves aside and closes in behind the vehicle. As a result, the body behaves as though it possesses more mass than it actually does, giving rise to the phenomenon commonly referred to as added mass. Assuming potential flow of an irrotational frictionless fluid, the mass matrix of the surrounding fluid is symmetric [19]. That is, $M_V^A = (M_V^A)^\mathsf{T}$, and the added mass matrix requires, at most, 21 independent constants

$$M_V^A = \begin{bmatrix} X_{\dot{u}} & X_{\dot{v}} & X_{\dot{w}} & X_{\dot{p}} & X_{\dot{q}} & X_{\dot{r}} \\ X_{\dot{v}} & Y_{\dot{v}} & Y_{\dot{w}} & Y_{\dot{p}} & Y_{\dot{q}} & Y_{\dot{r}} \\ X_{\dot{w}} & Y_{\dot{w}} & Z_{\dot{w}} & Z_{\dot{p}} & Z_{\dot{q}} & Z_{\dot{r}} \\ X_{\dot{p}} & Y_{\dot{p}} & Z_{\dot{p}} & K_{\dot{p}} & K_{\dot{q}} & K_{\dot{r}} \\ X_{\dot{q}} & Y_{\dot{q}} & Z_{\dot{q}} & K_{\dot{q}} & M_{\dot{q}} & M_{\dot{r}} \\ X_{\dot{r}} & Y_{\dot{r}} & Z_{\dot{r}} & K_{\dot{r}} & M_{\dot{r}} & N_{\dot{r}} \end{bmatrix}. \tag{2.19}$$

Since M_V^A is accounted for on the right-hand side of the vehicle dynamics (2.14), the mass matrix is negative definite $M_V^A < 0$ [8, Ch. 2]. The kinetic energy of the fluid expressed in

quadratic form is

$$T_V^A = -\frac{1}{2}\nu^\mathsf{T} M_V^A \nu, \tag{2.20}$$

Kirchhoff's equations [23] relate the force vector $\tau_1 = [X^A, Y^A, Z^A]^\mathsf{T}$ and moment vector $\tau_2 = [K^A, M^A, N^A]^\mathsf{T}$ to the kinetic energy of the fluid

$$\tau_1 = \frac{d}{dt}\left(\frac{\partial T_V^A}{\partial \nu_1}\right) + \nu_2 \times \frac{\partial T_V^A}{\partial \nu_1} \tag{2.21}$$

$$\tau_2 = \frac{d}{dt}\left(\frac{\partial T_V^A}{\partial \nu_2}\right) + \nu_2 \times \frac{\partial T_V^A}{\partial \nu_2} + \nu_1 \times \frac{\partial T_V^A}{\partial \nu_1}. \tag{2.22}$$

The force τ_1 and moment τ_2 vectors can be expressed in matrix form

$$\begin{bmatrix} \tau_1 \\ \tau_2 \end{bmatrix} = \tau_V^A = M_V^A \dot{\nu} + C_V^A(\nu)\nu, \tag{2.23}$$

as shown by Fossen [8, Ch. 2.4]. The mass matrix of the surrounding fluid M_V^A is defined in (2.19), and the Coriolis matrix is

$$C_V^A(\nu) = \begin{bmatrix} 0 & 0 & 0 & 0 & a_3 & -a_2 \\ 0 & 0 & 0 & -a_3 & 0 & a_1 \\ 0 & 0 & 0 & a2 & -a_1 & 0 \\ 0 & a_3 & -a_2 & 0 & b_3 & -b_2 \\ -a_3 & 0 & a_1 & -b_3 & 0 & b_1 \\ a_2 & -a_1 & 0 & b_2 & -b_1 & 0 \end{bmatrix}, \tag{2.24}$$

where

$$\begin{aligned} a_1 &= X_{\dot{u}}u + X_{\dot{v}}v + X_{\dot{w}}w + X_{\dot{p}}p + X_{\dot{q}}q + X_{\dot{r}}r \\ a_2 &= X_{\dot{v}}u + Y_{\dot{v}}v + Y_{\dot{w}}w + Y_{\dot{p}}p + Y_{\dot{q}}q + Y_{\dot{r}}r \\ a_3 &= X_{\dot{w}}u + Y_{\dot{w}}v + Z_{\dot{w}}w + Z_{\dot{p}}p + Z_{\dot{q}}q + Z_{\dot{r}}r \\ b_1 &= X_{\dot{p}}u + Y_{\dot{p}}v + Z_{\dot{p}}w + K_{\dot{p}}p + K_{\dot{q}}q + K_{\dot{r}}r \\ b_2 &= X_{\dot{q}}u + Y_{\dot{q}}v + Z_{\dot{q}}w + K_{\dot{q}}p + M_{\dot{q}}q + M_{\dot{r}}r \\ b_3 &= X_{\dot{r}}u + Y_{\dot{r}}v + Z_{\dot{r}}w + K_{\dot{r}}p + M_{\dot{r}}q + N_{\dot{r}}r \end{aligned} . \tag{2.25}$$

For a conventional streamline vehicle, many of the added mass coefficients are negligible due to the vehicle possessing top/bottom and port/starboard symmetry [8, Ch. 2.5]. In particular, the mass matrix corresponding to the surrounding fluid reduces to

$$M_V^A = \begin{bmatrix} X_{\dot{u}} & 0 & 0 & 0 & 0 & 0 \\ 0 & Y_{\dot{v}} & 0 & 0 & 0 & Y_{\dot{r}} \\ 0 & 0 & Z_{\dot{w}} & 0 & Z_{\dot{q}} & 0 \\ 0 & 0 & 0 & K_{\dot{p}} & 0 & 0 \\ 0 & 0 & Z_{\dot{q}} & 0 & M_{\dot{q}} & 0 \\ 0 & Y_{\dot{r}} & 0 & 0 & 0 & N_{\dot{r}} \end{bmatrix}, \tag{2.26}$$

and the Coriolis matrix reduces to

$$C_V^A(\nu) = -\begin{bmatrix} 0 & 0 & 0 & 0 & Z_{\dot{w}}w + Z_{\dot{q}}q & -(Y_{\dot{v}}v + Y_{\dot{r}}r) \\ 0 & 0 & 0 & -(Z_{\dot{w}}w + Z_{\dot{q}}q) & 0 & X_{\dot{u}}u \\ 0 & 0 & 0 & Y_{\dot{v}}v + Y_{\dot{r}}r & -X_{\dot{u}}u & 0 \\ 0 & Z_{\dot{w}}w + Z_{\dot{q}}q & -(Y_{\dot{v}}v + Y_{\dot{r}}r) & 0 & Y_{\dot{r}}v + N_{\dot{r}}r & -(Z_{\dot{q}}w + M_{\dot{q}}q) \\ -(Z_{\dot{w}}w + Z_{\dot{q}}q) & 0 & X_{\dot{u}}u & -(Y_{\dot{r}}v + N_{\dot{r}}r) & 0 & K_{\dot{p}}p \\ Y_{\dot{v}}v + Y_{\dot{r}}r & -X_{\dot{u}}u & 0 & Z_{\dot{q}}w + M_{\dot{q}}q & -K_{\dot{p}}p & 0 \end{bmatrix}. \tag{2.27}$$

The added mass coefficients for vehicle will have contributions from the body and control fins. One approach for obtaining the added mass coefficients for the body contribution is to approximate the body as a prolate spheroid. Lamb presents closed-form analytic expressions for the added mass coefficients of a prolate spheroid [24, Ch. 6]

$$X_{\dot{u}_b} = -\frac{\alpha_0}{2-\alpha_0} m_f, \tag{2.28}$$

$$Z_{\dot{w}_b} = Y_{\dot{v}_b} = -\frac{\beta_0}{2-\beta_0} m_f, \tag{2.29}$$

$$K_{\dot{p}_b} = 0, \tag{2.30}$$

$$Z_{\dot{q}_b} = Y_{\dot{r}_b} = 0, \tag{2.31}$$

$$M_{\dot{q}_b} = N_{\dot{r}_b} = -\frac{1}{5}\frac{(b^2-a^2)(\alpha_0-\beta_0)}{2(b^2-a^2)+(b^2+a^2)(\beta_0-\alpha_0)} m_f. \tag{2.32}$$

The dimensions of the prolate spheroid are defined in Figure 2.3. The mass of the fluid displaced by the prolate spheroid is

$$m_f = \frac{4}{3}\pi\rho a b^2, \tag{2.33}$$

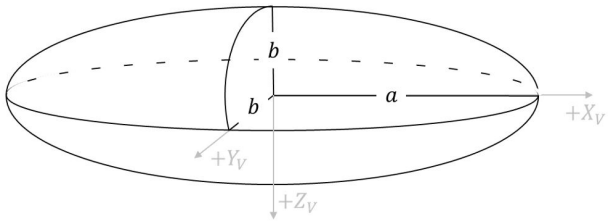

Figure 2.3: Prolate spheroid of length $2a$ and radius b

where ρ denotes the fluid density. The constants β_0 and α_0 are calculated from

$$\alpha_0 = \frac{2(1-e^2)}{e^3}\left(\frac{1}{2}\ln\frac{1+e}{1-e} - e\right), \tag{2.34}$$

$$\beta_0 = \frac{1}{e^2} - \frac{1-e^2}{2e^3}\ln\frac{1+e}{1-e}, \tag{2.35}$$

where the eccentricity of the ellipse is

$$e = \sqrt{1-(b/a)^2}. \tag{2.36}$$

When the hull is approximated by a prolate spheroid, eqs. (2.28) to (2.32) are used to calculate the added mass coefficients of the body.

Alternatively, the added mass coefficients of a hull can be approximated by employing strip theory. This approach has been employed for slender ships and underwater vehicles [5], [27], [28]. To yield a reasonably accurate approximation from slender body theory, Newman suggests the diameter-length ratio of 0.1 to 0.2 as an upper limit for a submerged body [27, Ch. 7]. Strip theory approximates the added mass effect by dividing the hull into thin strips, calculating the two-dimensional added mass effect for each strip, and integrating the effects of each strip along the length of the vehicle to obtain the three-dimensional added mass coefficient.

For a slender body, Newman [27] found that the added mass in the longitudinal direction

$X_{\dot{u}_b}$ is negligible compared to the vehicle's dry mass m_v. Furthermore, the approximation of $X_{\dot{u}_b}$ is prohibitively complex to compute, and provides little improvement in accuracy compared to the axial added mass coefficient of a prolate spheroid having the same length and diameter as the vehicle. Therefore, when calculating the axial added mass coefficient for a vehicle with the assumed geometry of a Myring profile, equation (2.28) is used.

For an axisymmetric body about the longitudinal axis, the coefficient of rolling added mass is zero, $k_{\dot{p}_b} = 0$. For lateral and rotary motion, the added mass coefficients are calculated

$$Z_{\dot{w}_b} = Y_{\dot{v}_b} = -\rho \int_{x_{t_1}}^{x_{n_2}} \pi R_b^2(x) dx, \tag{2.37}$$

$$-Z_{\dot{q}_b} = Y_{\dot{r}_b} = -\rho \int_{x_{t_1}}^{x_{n_2}} \pi R_b^2(x) x dx, \tag{2.38}$$

$$M_{\dot{q}_b} = N_{\dot{r}_b} = -\rho \int_{x_{t_1}}^{x_{n_2}} \pi R_b^2(x) x^2 dx, \tag{2.39}$$

where x_{t_1} and x_{n_2} specify the axial position of the aft end of the tail section and the bow end of the nose section, respectively. Strip theory is used to calculate the added mass coefficients of the body when its geometry is modeled by a Myring profile, where $R_b(x)$ is given by (2.13).

The influence of control fins can be accounted for by approximating the fins as flat plates. Based on the formulations compiled by Humphreys and Watkinson [17], the added mass contributions of four identically sized fins that have chord length c and span b that are placed in a cruciform configuration are presented

$$Z_{\dot{w}_f} = Y_{\dot{v}_f} = -2(k_p \frac{1}{4} \rho \pi c^2 b), \tag{2.40}$$

$$-Z_{\dot{q}_f} = Y_{\dot{r}_f} = Y_{\dot{v}_f} x_f, \tag{2.41}$$

$$M_{\dot{q}_f} = N_{\dot{r}_f} = -2(k'_p \frac{1}{48} \rho \pi c^3 b^2) + Y_{\dot{v}_f} x_f^2, \tag{2.42}$$

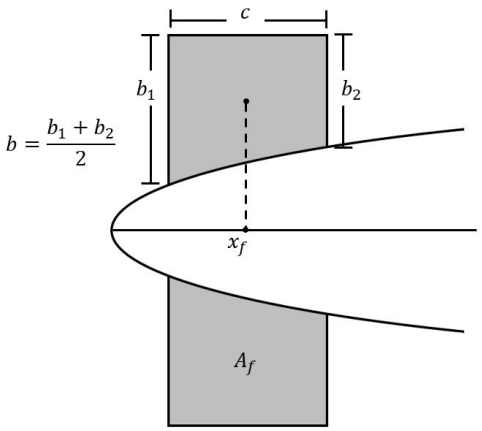

Figure 2.4: Dimensions for a pair of identically sized control fins

where x_f specifies the axial position of the fin centroid along the vehicle, referenced from the vehicle origin. The first term on the RHS of (2.42) is the moment of inertia for the rotation about an axis parallel to the fin span located at midchord, and the second term is the moment of inertia for the rotation about the Z_V and Y_V axes of the vehicle for $N_{\dot{r}_f}$ and $M_{\dot{q}_f}$, respectively. The coefficient of additional mass for a flat plate is

$$k_p = \frac{1}{\sqrt{1 + 1/AR}}. \tag{2.43}$$

The aspect ratio AR is a function of the fin area A_f and is defined as $AR = b^2/A_f$. The definitions of the fin dimensions are illustrated in Figure 2.4. The coefficient of additional moment of inertia is denoted by k'_p, whereby the value is obtained from empirical results for flat plates with varying aspect ratios. Gracey presents the experimental findings in [12], and for convenience, the results are replicated in Figure 2.5.

The rolling added mass coefficient due to the influence of the control fins is calculated in a manner that parallels the calculation of $M_{\dot{q}_f} = N_{\dot{r}_f}$. The additional roll moment of inertia accounts for the rotation about an axis parallel to the fin chord located at midspan, along with accounting for the rotation about the X_V axis. Taking into account all four control

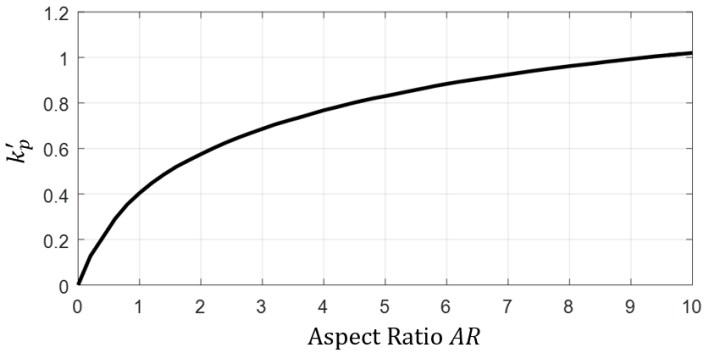

Figure 2.5: Coefficient of additional moment of inertia for a flat plate

surfaces, the coefficient is

$$K_{\dot{p}_f} = -4(k'_p \frac{1}{48} \rho \pi c^2 b^3) + 2(Y_{\dot{v}_f} y_f^2), \tag{2.44}$$

with y_f denoting the height of the fin centroid relative to the vehicle center line [12]. The added mass coefficients for the vehicle are obtained by summing the body contributions and the fin contributions

$$X_{\dot{u}} = X_{\dot{u}_b}, \tag{2.45}$$

$$Z_{\dot{w}} = Y_{\dot{v}} = Y_{\dot{v}_b} + Y_{\dot{v}_f}, \tag{2.46}$$

$$K_{\dot{p}} = K_{\dot{p}_f} \tag{2.47}$$

$$-Z_{\dot{q}} = Y_{\dot{r}} = Y_{\dot{r}_b} + Y_{\dot{r}_f}, \tag{2.48}$$

$$M_{\dot{q}} = N_{\dot{r}} = N_{\dot{r}_b} + N_{\dot{r}_f}. \tag{2.49}$$

2.3.3 Hyrdodynamic Damping and Control Forces and Moments

The hydrodynamic damping and control forces and moments that appear on the right-hand side of (2.14) are derived from the hydrodynamic lift and drag acting on the vehicle.

Vehicle Lift

When referring to the square of the vehicle diameter as the reference area $A_r = d_v^2$, Hoerner [15, pgs. 13-2 - 13-4] models the sideslip induced lift force acting on the body of the vehicle using the formula

$$Y_b = -\frac{1}{2}\rho A_r C_{yd} u^2, \tag{2.50}$$

where the subscript b is used to denote the lift contribution from the body of the vehicle. Hoerner formulates the lift coefficient C_{yd} with respect to the sideslip angle β in units of degrees. To facilitate analysis, the lift coefficient is presented with respect to β in units of radians

$$C_{yd} = \frac{dC_{yd}}{d\beta}\beta = \underbrace{\left(\frac{180}{\pi}\right)0.003\left(\frac{l_v}{d_v}\right)}_{c_{yd\beta}}\beta. \tag{2.51}$$

Provided that the surge and sway velocities satisfy $|u| \gg |v|$, the sideslip angle is approximated by invoking the small angle approximation

$$\beta \approx \tan(\beta) = \frac{v}{u}. \tag{2.52}$$

Substituting (2.52) and (2.51) into (2.50) results in

$$Y_b = -\frac{1}{2}\rho A_r c_{yd\beta}(uv). \tag{2.53}$$

Given that the vehicle's xz projection mirrors xy projection, the derivation of the lift force due to a sideslip angle can be extended to the lift due to an angle of attack $\alpha \approx \frac{w}{u}$ such that

$$Z_b = -\frac{1}{2}\rho A_r c_{yd\beta}(uw). \tag{2.54}$$

Equations (2.53) and (2.54) yield the lift force coefficients

$$Z_{uw_b} = Y_{uv_b} = -\frac{1}{2}\rho A_r c_{yd\beta}. \tag{2.55}$$

For a round body with fine-ness ratio $5 < l_v/d_v \leq 10$, the lateral force is centered along the latter half of the body. Hoerner found that the lift force acts at a axial location between 0.6 and 0.7 of the length, as referenced from the nose of the vehicle [15, pg. 13-4]. We select the location where the lift force is applied as the average of the location suggested in [15, pg. 13-4]. That is, we assign $x_b = x_{n2} - 0.65 l_v$ along the body, referenced from the origin of the vehicle. Using this location as the moment arm, the moments induced from the body lift force are

$$M_b = -Z_b \cdot x_b, \tag{2.56}$$

$$N_b = Y_b \cdot x_b. \tag{2.57}$$

Thus from (2.56) and (2.57), the lift moment coefficients are

$$-M_{uw_b} = N_{uv_b} = -\frac{1}{2}\rho A_r c_{yd\beta} x_b. \tag{2.58}$$

The lift force acting on an individual control surface is modeled using the formula from Hoerner [15, pg. 2-8]

$$Y_f = -\frac{1}{2}\rho A_f C_L(\beta_e) u^2, \tag{2.59}$$

where the lift coefficient for a wing is formulated with respect to β_e expressed in units of radians

$$C_L(\beta_e) = \underbrace{\left(\frac{2\bar{a}\pi}{1 + 2\bar{a}/AR_e}\right)}_{C_{L\alpha}} \beta_e, \tag{2.60}$$

where $\bar{a} = 0.9$, and the effective aspect ratio of the fin is defined as $AR_e = \left(2\frac{b^2}{A_f}\right)$.

The lift force of a fin is assumed to act at the centroid of the fin. For the lower and upper control surfaces, the centroid is specified by the local vehicle position vectors

$$\mathrm{p}_V^{f_l} = \begin{bmatrix} x_{f_l}, & 0, & z_{f_l} \end{bmatrix}^\mathsf{T}, \qquad \mathrm{p}_V^{f_u} = \begin{bmatrix} x_{f_u}, & 0, & z_{f_u} \end{bmatrix}^\mathsf{T}, \tag{2.61}$$

where $x_{f_u} = x_{f_l} = x_f$ and $-z_{f_u} = z_{f_l} = z_f$. For the case when both the upper and lower control surfaces operate in unison such that the control input to both fins is the rudder deflection angle δ_r, the effective sideslip angle for the lower and upper fins is defined as

$$\beta_{e_l} = \beta_{f_l} - \delta_r, \qquad \beta_{e_u} = \beta_{f_u} - \delta_r. \tag{2.62}$$

The sign convention for the angles is depicted in Figure 2.6. Since the fins are located at an offset from the vehicle origin, they experience the following velocities due to vehicle motion

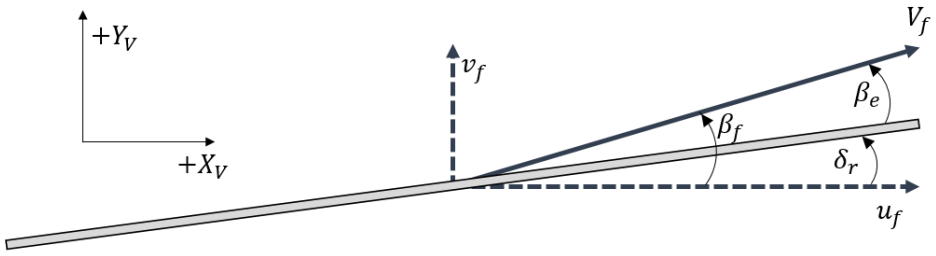

Figure 2.6: Sign convention for angles related to the upper and lower control surfaces

$$\mathrm{v}_V^{f_l} = \nu_1 + \nu_2 \times \mathrm{p}_V^{f_l}, \qquad \mathrm{v}_V^{f_u} = \nu_1 + \nu_2 \times \mathrm{p}_V^{f_u},$$

$$\begin{bmatrix} u_{f_l} \\ v_{f_l} \\ w_{f_l} \end{bmatrix} = \begin{bmatrix} u + z_f q \\ v + x_f r - z_f p \\ w - x_f q \end{bmatrix}, \qquad \begin{bmatrix} u_{f_u} \\ v_{f_u} \\ w_{f_u} \end{bmatrix} = \begin{bmatrix} u - z_f q \\ v + x_f r + z_f p \\ w - x_f q \end{bmatrix}.$$

For $|u_f| \gg |v_f|$, the sideslip angle experienced by the fin is obtained via the small angle approximation

$$\beta_{f_l} \approx \frac{v_{f_l}}{u_{f_l}} = \frac{v + x_f r - z_f p}{u + z_f q} \qquad \beta_{f_u} \approx \frac{v_{f_u}}{u_{f_u}} = \frac{v + x_f r + z_f p}{u - z_f q} \tag{2.63}$$

Inserting (2.63) into the effective sideslip angle (2.62), and calculating the net lift force (2.59) of both control surfaces, while assuming $|u| \gg |z_f q|$ yields

$$\begin{aligned} Y_f &= -\frac{1}{2}\rho A_f C_{L\alpha}\left(\frac{2v + 2x_f r}{u} - 2\delta_r\right)u^2 \\ &= -\rho A_f C_{L\alpha}(uv + x_f ur - u^2\delta_r). \end{aligned} \tag{2.64}$$

Given that the control surfaces are oriented in a cruciform configuration along the longitudinal axis of the body, the derivation of the lift force acting on the lower and upper control surfaces can be carried out for the starboard and port control surfaces whose centroids are

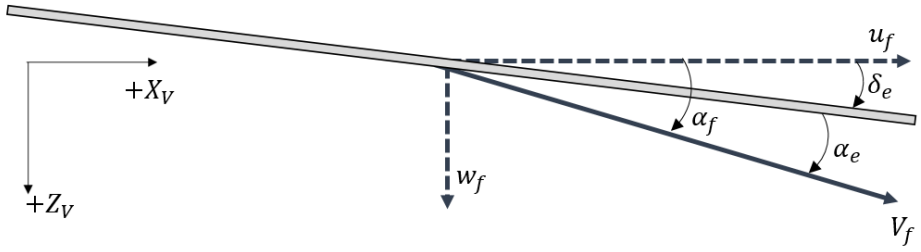

Figure 2.7: Sign convention for angles related to the port and starboard control surfaces

positioned at

$$\mathrm{p}_V^{f_s} = \begin{bmatrix} x_{f_s}, & y_{f_s}, & 0 \end{bmatrix}^\mathsf{T}, \qquad \mathrm{p}_V^{f_p} = \begin{bmatrix} x_{f_p}, & y_{f_p}, & 0 \end{bmatrix}^\mathsf{T}, \tag{2.65}$$

with $x_{f_p} = x_{f_s} = x_f$ and $-y_{f_p} = y_{f_s} = y_f$. The vertical fin lift force Z_f induced by an effective angle of attack $\alpha_e = \alpha_f - \delta_e$ is

$$Z_f = -\rho A_f C_{L\alpha}(uw - x_f uq - u^2\delta_e), \tag{2.66}$$

where the input elevator deflection angle is δ_e. The sign convention for α_e, α_f, and δ_e can be found in Figure 2.7. The coefficients resulting from (2.66) and (2.64) are

$$Z_{uw_f} = Y_{uv_f} = -2(\frac{1}{2}\rho A_f C_{L\alpha}), \tag{2.67}$$

$$-Z_{uq_f} = Y_{ur_f} = -2(\frac{1}{2}\rho A_f C_{L\alpha} x_f), \tag{2.68}$$

$$Z_{uu\delta_e} = Y_{uu\delta_r} = 2(\frac{1}{2}\rho A_f C_{L\alpha}). \tag{2.69}$$

The moments induced by fin lift are

$$M_f = -Z_f \cdot x_f, \qquad N_f = Y_f \cdot x_f, \tag{2.70}$$

yielding the lift induced moment coefficients

$$-M_{uwf} = N_{uvf} = -2(\frac{1}{2}\rho A_f C_{L\alpha} x_f), \tag{2.71}$$

$$M_{uqf} = N_{urf} = -2(\frac{1}{2}\rho A_f C_{L\alpha} x_f^2), \tag{2.72}$$

$$-M_{uu\delta e} = N_{uu\delta r} = 2(\frac{1}{2}\rho A_f C_{L\alpha} x_f). \tag{2.73}$$

The net coefficients for the vehicle are obtained by summing the body and the fin contributions

$$Z_{uw} = Y_{uv} = Y_{uvb} + Y_{uvf}, \tag{2.74}$$

$$-Z_{uq} = Y_{ur} = Y_{urf}, \tag{2.75}$$

$$-M_{uw} = N_{uv} = N_{uvb} + N_{uvf}, \tag{2.76}$$

$$M_{uq} = N_{ur} = N_{urf}. \tag{2.77}$$

Vehicle Drag

The drag force acting on the vehicle consists of the axial drag force and the crossflow drag forces. The axial drag acting on a streamlined body is modeled by Hoerner [14] as

$$D = \underbrace{-\frac{1}{2}\rho C_D A_{fr}}_{X_{|u|u_b}} |u|u, \tag{2.78}$$

where the frontal area of the vehicle is $A_{fr} = \pi r_v^2$. The selection of the drag coefficient is dependent on the Reynold's number of the vehicle

$$R_l = \frac{u l_v}{\nu}, \tag{2.79}$$

where ν, not to be confused with the local body velocity vector, is the fluid's kinematic viscosity. For fresh water at 20°C, $\nu = 10.04 \times 10^{-}7\ m^2/s$ [3]. The SATLP vehicle is designed to operate at a nominal surge speed of $u = 2m/s$, yielding the Reynold's number $R_l = 1.66 \times 10^6$. The corresponding drag coefficient in turbulent flow $R_l \geq 10^6$ is given by Hoerner [14, pg. 6-18] as

$$C_D = C_f \left[3\Big(\frac{l_v}{d_v}\Big) + 4.5\Big(\frac{d_v}{l_v}\Big)^{1/2} + 7\Big(\frac{l_v}{d_v}\Big)^2 \right], \tag{2.80}$$

where the friction drag coefficient is approximately $C_f = 0.004$ [14, pg. 3-12].

Based on the total wetted area, the contribution of the fins to the axial drag is

$$X_{|u|u_f} = -4\left(\frac{1}{2}\rho C_{D_0} 2A_f\right). \tag{2.81}$$

For control surfaces having a geometric profile of a NACA 0009 airfoil, the parasitic drag coefficient is $C_{D_0} = 0.0055$ [1]. The net axial drag coefficient is obtained by summing the body and fin contribution

$$X_{|u|u} = X_{|u|u_b} + X_{|u|u_f}. \tag{2.82}$$

The method to calculate the coefficients resulting from crossflow drag parallels the strip theory method used to calculate the added mass coefficients presented in Section 2.3.2. The differential crossflow drag force acting on a differential area of the vehicle induced by a pure sway velocity is depicted in Figure 2.8, where

$$\delta Y = -\frac{1}{2}\rho c_d \underbrace{2R(x)\delta x}_{\delta A} |v|v. \tag{2.83}$$

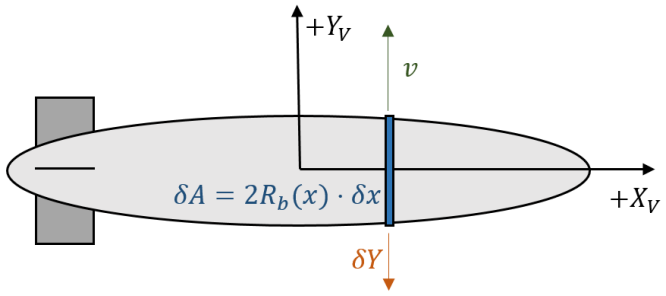

Figure 2.8: Differential crossflow drag force acting on a differential area of the vehicle induced by a pure translational velocity

Integrating (2.83) along the length of the vehicle yields

$$Y = -\frac{1}{2}\rho c_{dc}\int_{x_{t1}}^{x_{n2}} 2R_b(x)\delta x|v|v - \frac{1}{2}\rho c_{df}\int_{x_{f1}}^{x_{f2}} 2(R_f(x) - R_b(x))\delta x|v|v \tag{2.84}$$

resulting in the following coefficients for an axisymmetric body

$$Z_{|w|w} = Y_{|v|v} = -\frac{1}{2}\rho c_{dc}\int_{x_{t1}}^{x_{n2}} 2R_b(x)\delta x - \frac{1}{2}\rho c_{df}\int_{x_{f1}}^{x_{f2}} 2(R_f(x) - R_b(x))\delta x, \tag{2.85}$$

where the crossflow drag coefficient for a cylinder is given by Hoerner [15, pg. 3-2] as $c_{dc} = 1.2$. Additionally, from Hoerner [15, pg. 3-15] the value for crossflow drag coefficient for a square flat plate is taken to be $c_{df} = 1.17$. The corresponding induced differential moments are

$$\delta N = \delta Y \cdot x, \qquad \delta M = -\delta Z \cdot x. \tag{2.86}$$

By integrating over the length of the vehicle, the total moment is obtained, and the resulting coefficients are

$$-M_{|w|w} = N_{|v|v} = -\frac{1}{2}\rho c_{dc}\int_{x_{t1}}^{x_{n2}} 2R_b(x)x\delta x - \frac{1}{2}\rho c_{df}\int_{x_{f1}}^{x_{f2}} 2(R_f(x) - R_b(x))x\delta x. \tag{2.87}$$

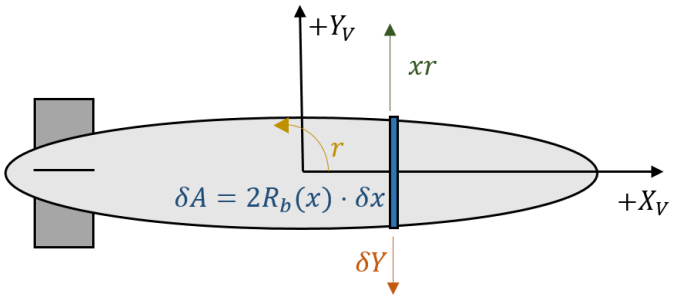

Figure 2.9: Differential crossflow drag force acting on a differential area of the vehicle induced by a rotational velocity

The differential crossflow drag force induced by a pure rotational velocity can be seen in Figure 2.9 where

$$\delta Y = -\frac{1}{2}\rho c_d \underbrace{2R(x)\delta x}_{\delta A} |xr|xr. \tag{2.88}$$

Since the vehicle's (xy) projection mirrors the (xz) projection, the integrations performed for the differential drag force induced by a pure sway velocity and pure angular rate r can be extended for the heave velocity and angular rate q, yielding the coefficients

$$-Z_{|q|q} = Y_{|r|r} = -\frac{1}{2}\rho c_{dc}\int_{x_{t1}}^{x_{n2}} 2R_b(x)x|x|\delta x - \frac{1}{2}\rho c_{df}\int_{x_{f1}}^{x_{f2}} 2(R_f(x) - R_b(x))x|x|\delta x, \tag{2.89}$$

$$M_{|q|q} = N_{|r|r} = -\frac{1}{2}\rho c_{dc}\int_{x_{t1}}^{x_{n2}} 2R_b(x)x^2|x|\delta x - \frac{1}{2}\rho c_{df}\int_{x_{f1}}^{x_{f2}} 2(R_f(x) - R_b(x))x^2|x|\delta x. \tag{2.90}$$

Similar expressions for crossflow drag coefficients appear in [28].

Lift and Drag Forces Expressed in Matrix Form

By defining the matrix

$$D(\nu) = \begin{bmatrix} X_{|u|u}|u| & 0 & 0 & 0 & 0 & 0 \\ 0 & Y_{|v|v}|v| + Y_{uv}u & 0 & 0 & 0 & Y_{|r|r}|r| + Y_{ur}u \\ 0 & 0 & Z_{|w|w}|w| + Z_{uw}u & 0 & Z_{|q|q}|q| + Y_{uq}u & 0 \\ 0 & 0 & 0 & K_{|p|p}|p| & 0 & 0 \\ 0 & 0 & M_{|w|w}|w| + M_{uw}u & 0 & M_{|q|q}|q| + M_{uq}u & 0 \\ 0 & N_{|v|v}|v| + N_{uv}u & 0 & 0 & 0 & N_{|r|r}|r| + N_{ur}u \end{bmatrix}, \tag{2.91}$$

the hydrodynamic damping and control forces can be expressed as

$$\tau_V^D + \tau_V^C = D(\nu)\nu + \begin{bmatrix} 1 & 0 & 0 \\ 0 & Y_{uu\delta_r}u^2 & 0 \\ 0 & 0 & Z_{uu\delta_e}u^2 \\ 0 & 0 & 0 \\ 0 & 0 & M_{uu\delta_e}u^2 \\ 0 & N_{uu\delta_r}u^2 & 0 \end{bmatrix} \begin{bmatrix} X_{prop} \\ \delta_r \\ \delta_e \end{bmatrix}, \tag{2.92}$$

where X_{prop} denotes the thrust from the propeller. For simplicity, the thrust is modeled as a constant force selected to achieve a steady-state surge speed of $2m/s$. In reality, any maneuvers in which the vehicle is not traveling at self-propulsion speed, the thrust force will deviate from the nominal value required to yield the desired steady state surge speed. More sophisticated methods of modeling the thrust force can be found in [8, 11, 32].

The hydrodynamic coefficients of a vehicle are obtained using a method consisting of analytic expressions, strip theory approximations, and experimental findings. The simplification introduced by the potential flow assumption, while enabling the estimation of coefficients

without resorting to computational fluid dynamics tool, neglects some of the physics that determine some of the hydrodynamic coefficients. For the case of strip theory approximations, the added mass force acting on any individual strip is simplified such that the force on a strip is not affected by any other strip along the vehicle. In the extreme case of a sphere, the sway added mass coefficient is over-predicted by 100% [27]. A more egregious error results for the added moment of inertia coefficient $N_{\dot{r}}$. For a sphere, slender body theory yields a non-zero result, however the analytic solution (2.32) reduces to zero for a sphere. This can be easily verified by setting $a = b$ in (2.32).

Additionally, we compute contributions from a body and from fins independently, and then sum the result. Interference affects between the body and fins are ignored. Hence, caution must be exercised when employing analytic and semi-empirical methods. As vehicle design progresses and becomes finalized, best practices systematically correct the analytic predictions such that better agreement is achieved with experimental findings [6, 7, 28, 30, 32].

In Chapter 3, forces and moments predicted by ASE coefficients, for a prescribed velocity and acceleration trajectory, are compared to those seen in high fidelity computational fluid dynamics simulations, providing a quantitative assessment on the utility and limitations of the coefficients derived from the ASE methods.

2.3.4 Restorative Forces and Moments

The forces due to gravity and buoyancy acting on the vehicle are referred to as the restorative forces. With respect to the inertial frame, the gravitational and buoyant forces are

$$F_I^G = \begin{bmatrix} 0, & 0, & m_v g \end{bmatrix}^\mathsf{T}, \qquad F_I^B = \begin{bmatrix} 0, & 0, & -\rho \nabla g \end{bmatrix}^\mathsf{T}. \tag{2.93}$$

Given that the Z_I-axis is defined as positive downwards, the acceleration due to gravity is $g = 9.81 m/s^2$. The volume of the displaced fluid is denoted ∇. To obtain the forces with respect to the local vehicle frame, the kinematic transformation is applied

$$F_V^G = (R_{IV}^{\eta_1})^{-1} F_I^G, \qquad F_V^B = (R_{IV}^{\eta_1})^{-1} F_I^B. \tag{2.94}$$

The gravitational force acts through the CG, located at r_V^G, and likewise the buoyant force acts through the CB located at r_V^B. The net force and moment with respect to the local vehicle reference frame is

$$g_V(\eta) = \begin{bmatrix} F_V^G + F_V^B \\ (r_V^G \times F_V^G) + (r_V^B \times F_V^B) \end{bmatrix}. \tag{2.95}$$

Chapter 3

Virtual Planar Motion Mechanism Simulations

The primary focus of this chapter is placed on assessing the coefficients obtained from the ASE methods developed in Chapter 2. This is done by comparing the measured forces and moments from virtual planar motion mechanism simulations to the predicted forces and moments from the ASE coefficients. This chapter concludes with the parameter estimation results of the hydrodynamic coefficients for the SATLP vehicle used for controller design and system simulation.

Gertler developed the planar motion mechanism (PMM) in an effort to experimentally determine the hydrodynamic coefficients for a submerged body [10]. The mechanism constrains motion of the body to either the dive plane (xz) or the steering plane (xy), and then prescribes a particular maneuver for the motion of the body. The body's hydrodynamic coefficients are then identified using the time histories of the maneuver and the measured forces and moments acting on the body.

For a vehicle constrained to the steering plane, the local velocity vector reduces to $\nu = \begin{bmatrix} u, & v, & r \end{bmatrix}^{\mathsf{T}}$. During a surge maneuver, the vehicle experiences no lateral or rotary motion

so that the velocity and acceleration vectors are

$$\nu = \begin{bmatrix} u + a_x\omega_x \cos(\omega_x t) \\ 0 \\ 0 \end{bmatrix}, \qquad \dot{\nu} = \begin{bmatrix} -a_x\omega_x^2 \sin(\omega_x t) \\ 0 \\ 0 \end{bmatrix}, \tag{3.1}$$

where u denotes the nominal surge speed. The amplitude and angular frequency of the oscillatory motion is specified a_x and ω_x, respectively. The external force acts solely along the longitudinal axis of the body and is modeled as

$$X_{ext} = X_{\dot{u}}\dot{u} + X_{|u|u}|u|u. \tag{3.2}$$

For a sway maneuver, the vehicle only experiences translational motion. The prescribed velocity and acceleration vectors are

$$\nu = \begin{bmatrix} u \\ -a_y\omega_y \cos(\omega_y t) \\ 0 \end{bmatrix}, \qquad \dot{\nu} = \begin{bmatrix} 0 \\ a_y\omega_y^2 \sin(\omega_y t) \\ 0 \end{bmatrix}. \tag{3.3}$$

The amplitude and angular frequency of the oscillatory motion is a_y and ω_y, respectively. Figure 3.1 illustrates the position and orientation of the vehicle throughout the sway maneuver. The resulting model for lateral force and yaw-axis moment acting on the vehicle is

$$\begin{aligned} Y_{ext} &= Y_{\dot{v}}\dot{v} + Y_{|v|v}|v|v + Y_{uv}uv, \\ N_{ext} &= Y_{\dot{r}}\dot{v} + N_{|v|v}|v|v + (N_{uv} + Y_{\dot{v}} - X_{\dot{u}})uv. \end{aligned} \tag{3.4}$$

For a yaw maneuver, the vehicle travels along a sinusoidal path and rotates such that the X_V

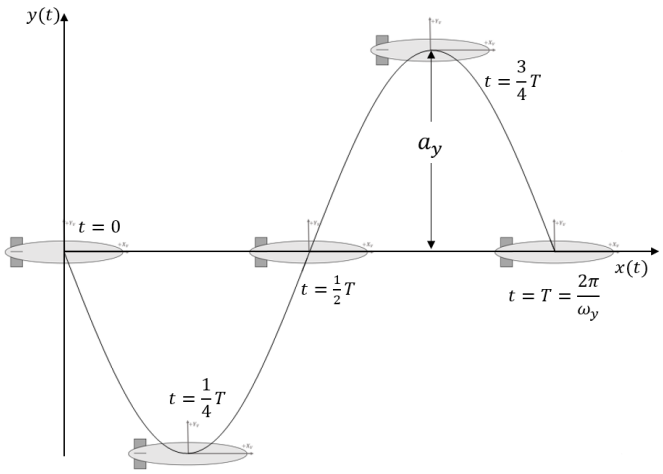

Figure 3.1: Vehicle position and orientation during a sway maneuver

axis is tangent to path, resulting in no lateral motion. Thus the velocity and acceleration vectors are

$$\nu = \begin{bmatrix} u \\ 0 \\ a_\psi \omega_\psi \sin(\omega_\psi t) \end{bmatrix}, \qquad \dot{\nu} = \begin{bmatrix} 0 \\ 0 \\ a_\psi \omega_\psi^2 \cos(\omega_\psi t) \end{bmatrix}. \tag{3.5}$$

The amplitude and angular frequency of the oscillatory yaw angle is a_ψ and ω_ψ, respectively. Figure 3.2 illustrates the position and orientation of the vehicle throughout the yaw maneuver. The lateral force and yaw-axis moment acting on the vehicle reduces to

$$\begin{aligned} Y_{ext} &= Y_{\dot{r}}\dot{r} + Y_{|r|r}|r|r + (Y_{ur} + X_{\dot{u}})ur, \\ N_{ext} &= N_{\dot{r}}\dot{r} + N_{|r|r}|r|r + (N_{ur} + Y_{\dot{r}})ur. \end{aligned} \tag{3.6}$$

A second-order model is standard in the underwater community[11], but other order models can also be used.

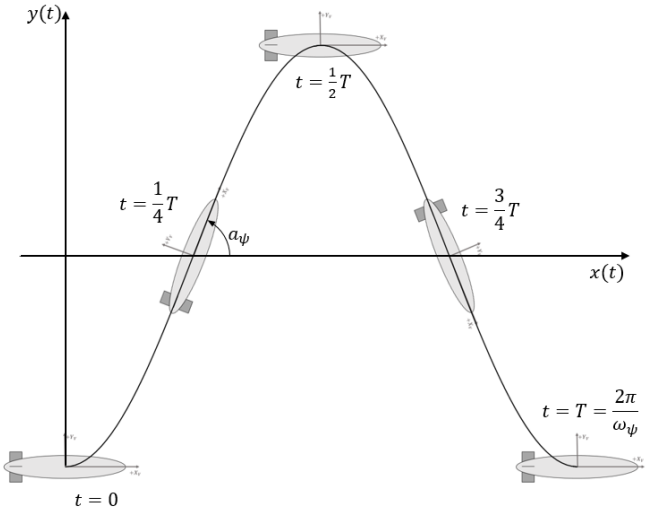

Figure 3.2: Vehicle position and orientation during a yaw maneuver

3.1 Continuous Least-Squares Estimation

Given the time histories of the measured forces and moments, and the time histories of the prescribed vehicle motion, the vehicle's coefficients can be identified using any standard parameter identification technique, specifically we select the continuous least-squares method.

Consider the linear parametric model

$$z(t) = \theta^{\mathsf{T}}(t)\phi(t), \tag{3.7}$$

where, $z(t) \in \mathbb{R}$, $\theta(t) \in \mathbb{R}^n$, $\phi(t) \in \mathbb{R}^n$ denote, at time t, the measurement, parameter estimate vector, and regressor vector, respectively. The number of parameters is denoted by n. The objective is to obtain the true parameter vector θ^* such that

$$J(\theta) = \frac{1}{2}\int_0^t ||z(\tau) - \theta^{\mathsf{T}}(\tau)\phi(\tau)||^2 d\tau \tag{3.8}$$

is minimized. From [20, Ch. 4.3], the update laws for the parameter estimate vector are

$$\dot{\theta}(t) = P(t)e(t)\phi(t), \qquad \theta(0) = \theta_0, \tag{3.9}$$

$$\dot{P}(t) = -P(t)\phi(t)\phi^{\mathsf{T}}(t)P(t), \qquad P(0) = P_0, \tag{3.10}$$

where the error between the measurement and the estimated measurement is $e(t) = z(t) - \theta^{\mathsf{T}}(t)\phi(t)$. The matrix $P(t) \in \mathbb{R}^{n\times n}$ is commonly referred to as the estimator gain matrix or the covariance matrix due the similarity of the least-squares algorithm and the Kalman filter. The update laws (3.9) and (3.10) guarantee that the parameters converge to constant values such that as $t \to \infty$, $\theta(t) \to \theta$. Provided that the time history of the regressor vector satisfies conditions for persistency of excitation, the parameter vector will converge to the true parameter vector, that is as $t \to \infty$, $\theta(t) \to \theta^*$. See [20] for further details on the persistency of excitation.

The constrained motion resulting from the PMM yields reduced linear parametric models for the force and moment acting on a vehicle. Consider a sway PMM manuever. The lateral force model reduces to

$$Y_{ext} = Y_{\dot{v}}\dot{v} + Y_{|v|v}|v|v + Y_{uv}uv, \tag{3.11}$$

which can alternatively be expressed as

$$\underbrace{Y_{ext}}_{z(t)} = \underbrace{\begin{bmatrix} Y_{\dot{v}}, & Y_{|v|v}, & Y_{uv} \end{bmatrix}}_{\theta^{\mathsf{T}}} \underbrace{\begin{bmatrix} \dot{v}, \\ |v|v, \\ uv \end{bmatrix}}_{\phi(t)}. \tag{3.12}$$

Given that the time histories of the PMM tests span a finite amount of time $t \in [0, T]$,

guaranteed convergence of the parameter vector $\theta(t)$ requires that the identification be implemented iteratively such that for each iteration, $P(t)$ and $\theta(t)$ are initialized with the final values from the previous iteration. For the k^{th} iteration, the parameter vector and estimator gain matrix are initialized as

$$\theta_k(0) = \theta_{k-1}(T), \qquad P_k(0) = P_{k-1}(T), \tag{3.13}$$

where the subscript denotes the iteration. This iterative identification procedure is carried out until $\theta(t)$ converges to a constant value. Thus the vehicle's coefficients are obtained by applying the iterative least-squares algorithm for each force and moment model resulting from the surge, sway, and yaw maneuvers.

Rather than perform captive tests with a physical model, an alternative approach is to numerically replicate the captive tests using CFD software. Virtual planar motion mechanism (VPMM) simulations are appealing due to the vast number of operating regimes under which the vehicle can be tested. Additionally, simulation-based methods are not hindered by the mechanical and physical limitations inherent with model testing [31].

3.2 Assessment of ASE methods

Assessment of hydrodynamic coefficients obtained from ASE methods is based on the accuracy of the predicted hydrodynamic forces and moments acting on:

1. An *idealized* underwater vehicle
2. An *actual* underwater vehicle.

The first case provides insight into the best possible agreement that can be achieved for an

ideal conventional vehicle, such as a prolate spheroid with fins at the tail. The second case evaluates how well the coefficients for an idealized body, such as a Myring profile with fins at the tail, predict the forces and moments acting on an actual vehicle whose geometric profile deviates from the Myring profile due to imperfections such as a blunt base, screw holes, etc.

A prolate spheroid is considered for the case of an idealized underwater vehicle. The spheroid was sized based on the max diameter and length of the SATLP. The control surfaces were sized to yield approximately the same area, and the fin centroid was placed at the same axial location. Sway and yaw maneuvers were performed for the finned prolate spheroid. The results of the sway maneuver are displayed in Figure 3.3.

The first row of plots shows the prescribed lateral velocity and acceleration of the vehicle. The first column of plots in second row shows the lateral force induced by lateral motion, where the first row is the force acting on the fin, the second row is the force acting on the body (hull), and the last row is the total force acting on the vehicle. The last column of plots shows the yaw-axis moment induced by lateral motion.

Satisfactory agreement is achieved for the lateral force. The yaw-axis moment, on the other hand, achieves satisfactory agreement in that the predicted and measured fin and body contributions are in phase, but the total moment shows poor agreement. The largest error for the moment acting on the body occurs when the acceleration is zero, implying that the velocity contribution to the moment is over predicted by the ASE coefficients. Conversely, the smallest errors result when the body velocity is zero, which is in accordance with the added mass coefficients being well predicted by potential flow theory.

The results of the yaw maneuver are displayed in Figure 3.4. The plots are organized in the same manner as the sway plots in Figure 3.3. Poor agreement is seen for the predicted lateral force and yaw-axis moment acting on the body. To further analyze the disagreement,

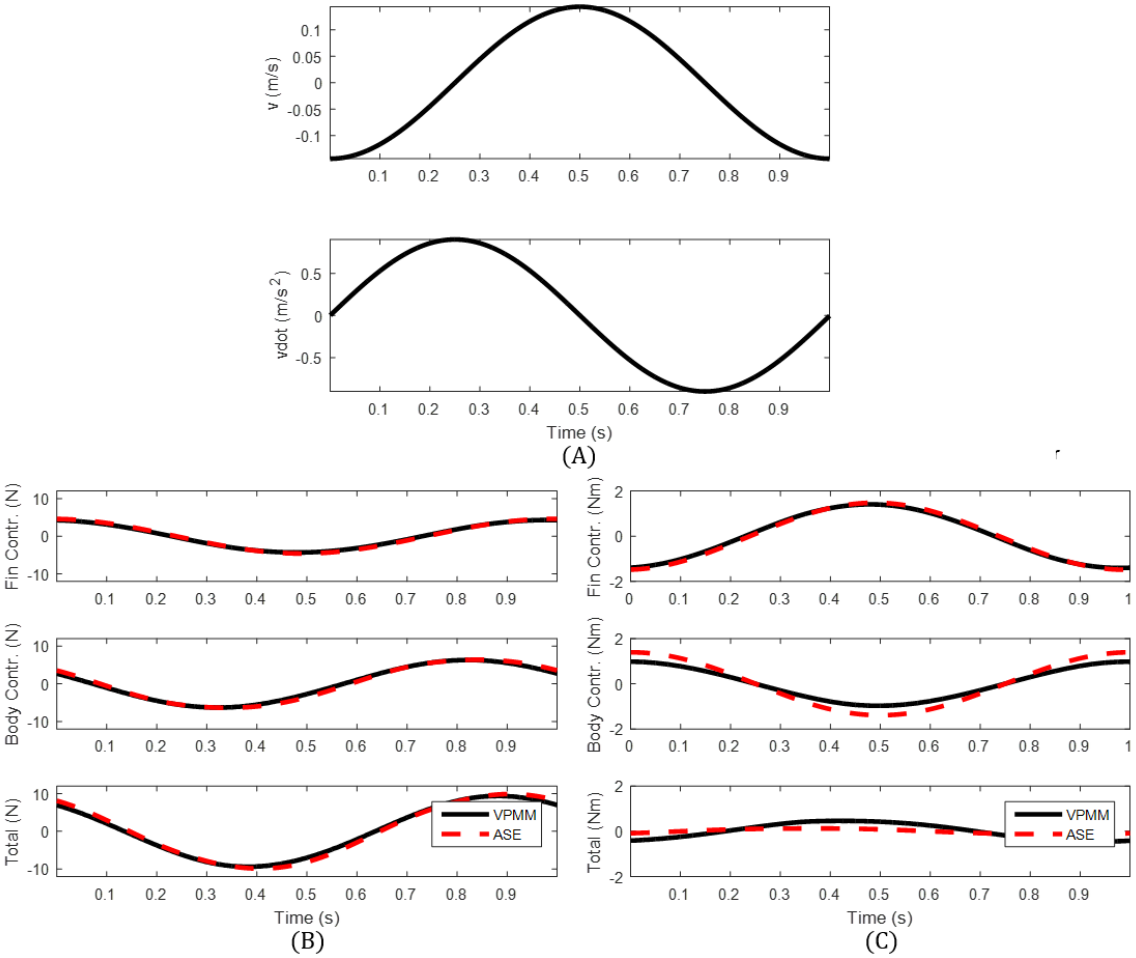

Figure 3.3: VPMM sway maneuver plots for prolate spheroid with fins placed at the tail. (A) Prescribed motion trajectories, (B) Lateral force comparison, (C) Yaw-axis moment comparison

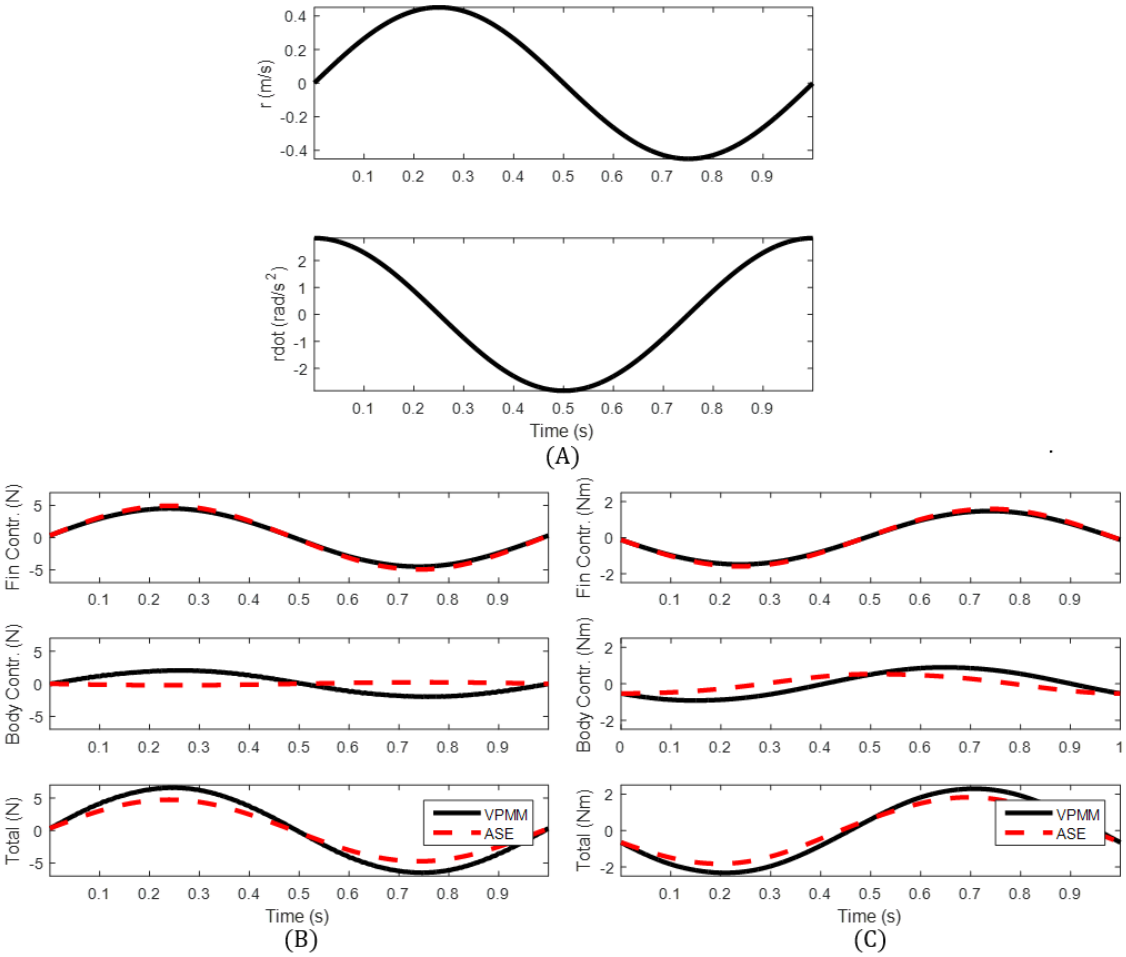

Figure 3.4: VPMM yaw maneuver plots for prolate spheroid with fins placed at the tail. (A) Prescribed motion trajectories, (B) Lateral force comparison, (C) Yaw-axis moment comparison

the force acting on the body is decomposed in to the contributions due to velocity and acceleration, as shown in Figure 3.5.

Recall the equation for a lateral force induced by rotary motion (3.6). For a prolate spheroid, potential flow theory yields $Y_{\dot{r}} = 0$, meaning that the lateral force acting on the body predicted by ASE coefficients will be due solely to forces induced by velocity. The velocity induced force is due to the velocity terms ur and $|r|r$. Given that that the surge speed takes on the constant value of $u = 2\ m/s$ for the entire simulation, the effect of the ur term will

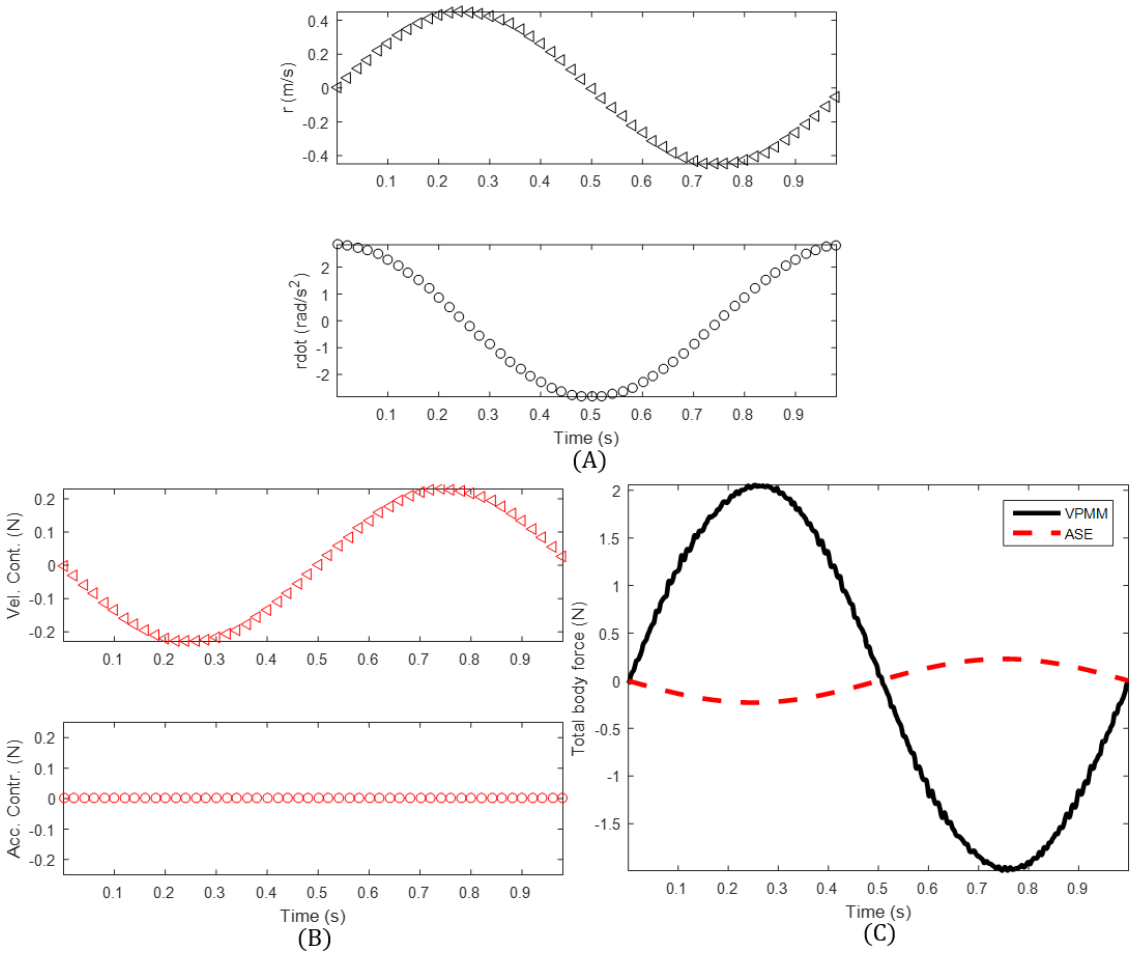

Figure 3.5: VPMM yaw maneuver plots for prolate spheroid with fins placed at the tail. (A) Prescribed motion trajectories, (B) Lateral force induced by velocity and acceleration acting on the body, (C) Net lateral force acting on the body

dominate the $|r|r$ term since r varies sinusoidally between $\pm 0.45\ rad/s$. The values of the coefficients that premultiply ur are

$$X_{\dot{u}_b} = -0.255, \qquad Y_{ur_b} = 0. \tag{3.14}$$

The coefficient $X_{\dot{u}_b}$ appears due to Coriolis forces, and its value is known with confidence from potential flow theory. The measured VPMM force is directly in phase with the velocity r, suggesting that the term $Y_{ur_b} \neq 0$. Expressions for the coefficients involving the surge

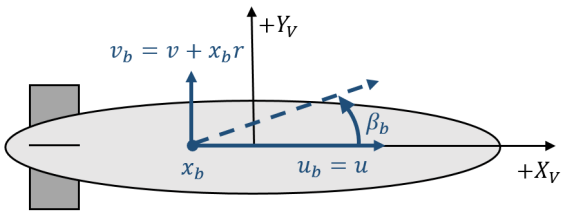

Figure 3.6: Local sideslip angle at the point at which the lift force is centered

velocity such as $Y_{uv_b}, N_{uv_b}, Y_{ur_b}, N_{ur_b}$, are derived from the lift acting on the body as proposed by Hoerner [15] based on data he gathered by for a non-rotating body. Thus the terms $Y_{ur_b} = N_{ur_b} = 0$.

One approach to yield better agreement between the ASE predictions and the VPMM data would be to derive the lift force acting acting on the body in a manner that parallels the derivation of the lift force acting on the control surfaces. Rather than developing the lift force (2.50) in terms of the vehicle sideslip angle β, consider development in terms of the local sideslip angle β_b, where β_b is the sideslip angle at the point x_b which the lateral force is centered along the body, such that the lift force (2.50) is modified to take the form

$$Y_b = -\frac{1}{2}\rho A_r (C_{yd\beta}\beta_b)u^2. \tag{3.15}$$

Using the small angle approximation, the local sideslip angle depicted in Figure 3.6 is approximately

$$\beta_b \approx \frac{v_b}{u_b} = \frac{v + x_b r}{u}. \tag{3.16}$$

Inserting the local sideslip angle into the modified lift force (3.15) and simplifying yields

$$Y_b = -\frac{1}{2}\rho A_r C_{yd\beta}(uv + x_b ur). \tag{3.17}$$

Using x_b as the moment arm, the moment induced by lift is

$$N_b = Y_b \cdot x_b. \tag{3.18}$$

Therefore the lift force and moment can be expressed in terms of the following coefficients

$$Y_{uv} = -\frac{1}{2}\rho A_r C_{yd\beta}, \tag{3.19}$$

$$Y_{ur} = -\frac{1}{2}\rho A_r C_{yd\beta} x_b, \tag{3.20}$$

$$N_{uv} = -\frac{1}{2}\rho A_r C_{yd\beta} x_b, \tag{3.21}$$

$$N_{ur} = -\frac{1}{2}\rho A_r C_{yd\beta} x_b^2. \tag{3.22}$$

These coefficients are calculated using the formulations for A_r, $C_{yd\beta}$, and x_b as described in Chapter 2.

Figure 3.7 contains the plots comparing the predicted lateral force and moment for $Y_{ur} = N_{ur} = 0$, and $Y_{ur} \neq 0, N_{ur} \neq 0$. Substantial improvement in agreement is achieved for the lateral force, while the yaw-axis moment sees no appreciable improvement. Once again, its worth remarking that the smallest errors between the VPMM and ASE predictions occur when the velocity is zero, implying good agreement among the added mass acceleration coefficients.

The values for $C_{yd\beta}$, and x_b as estimated by Hoerner [15] are based on experiments in which the the sideslip angle is induced by pure translational velocities. Thus extending the values for these parameters to rotary motion is not motivated by physics, however modeling body lift induced by rotary motion warrants further investigation.

The previous study of an idealized conventional tail-finned vehicle provides insight into the best possible agreement attainable. In practice, vehicles possess geometric imperfections,

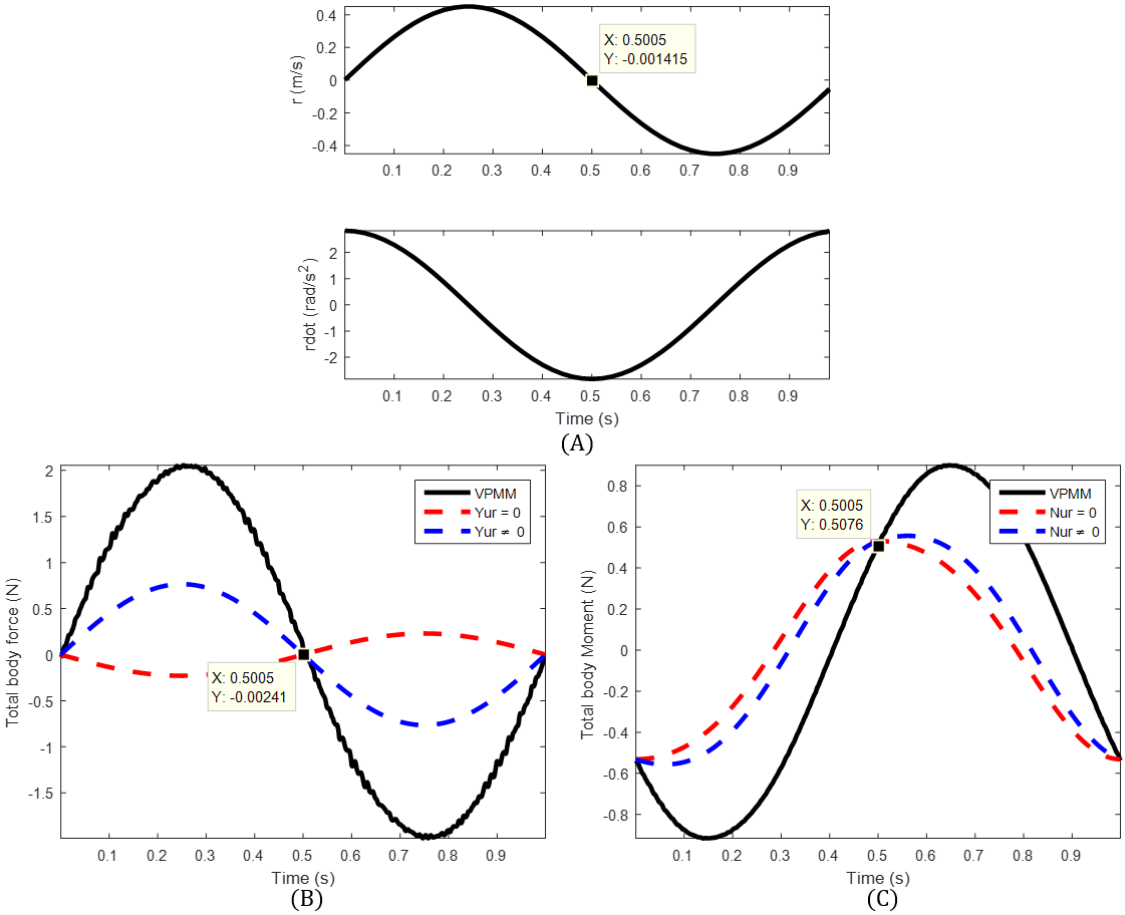

Figure 3.7: Comparison for $Y_{ur} = N_{ur} = 0$, and $Y_{ur} \neq 0, N_{ur} \neq 0$, (A) Motion trajectories, (B) Lateral force acting on the body, (C) Yaw-axis moment acting on the body

like screw holes, blunt bases, etc. that affect the flow field over the vehicle. When a vehicle is undergoing design iterations, it is desirable to approximate the vehicle's dynamic behavior to inform design considerations.

The next study seeks to assess how well the dynamics of actual vehicle can be approximated using a prolate spheroid or a Myring profile with control surfaces. This assessment is done by comparing the measured lateral force and yaw-axis moment acting on the SATLP vehicle with tail fins, to the force and moment predicted by the prolate spheroid coefficients and Myring vehicle coefficients.

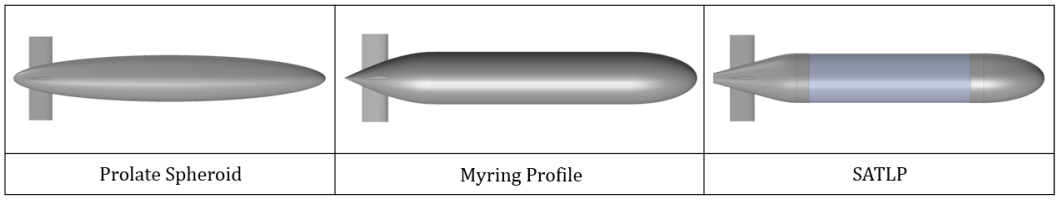

Figure 3.8: Vehicle profiles used in the study of a typical underwater vehicle

In an effort to maintain consistency across the three vehicles, the length and maximum diameter of both vehicles is the same as that of the SATLP. Additionally the area of the control surfaces were sized to yield approximately the same lifting force, with the centroid of the surfaces located at the same axial position along the vehicle as those of the SATLP. See Table A.2 for the fin parameters. Figure 3.8 provides an illustration of the vehicle geometries used for the study.

VPMM captive tests for surge, sway, and yaw maneuvers were simulated. The identified coefficients for the SATLP vehicle with tail fins are compared to the ASE coefficients for the prolate spheroid and Myring profile in Tables 3.1, 3.2, 3.3.

Table 3.1: Coefficients obtained from surge maneuver

Coefficient	Units	Prolate Spheroid	Myring Profile	SATLP
$X_{\dot{u}_b}$	kg	-0.2548	-0.2548	-0.4267
$X_{\dot{u}_f}$	kg	0.0000	0.0000	-0.0111
$X_{\dot{u}}$	kg	-0.2548	-0.2548	-0.4377
$X_{\|u\|u_b}$	kg/m	-0.5383	-0.5383	-0.5974
$X_{\|u\|u_f}$	kg/m	-0.1006	-0.1017	-0.1094
$X_{\|u\|u}$	kg/m	-0.6389	-0.6399	-0.7068

While the values of the coefficients are necessary to simulate the vehicle dynamics (2.14), more lucid insight on the utility of ASE coefficients in predicting the vehicle's dynamic behavior is gleaned by comparing the predicted forces and moments to the measured trajectories.

The plots in Figure 3.9 correspond to a sway maneuver, and the plots in 3.10 correspond to

Table 3.2: Coefficients obtained from sway maneuver

Coefficient	Units	Prolate Spheroid	Myring Profile	SATLP
$Y_{\dot{v}_b}$	kg	-6.2027	-8.1258	-7.5998
$Y_{\dot{v}_f}$	kg	-0.3296	-0.3360	-0.7621
$Y_{\dot{v}}$	kg	-6.5324	-8.4618	-8.3619
Y_{uv_b}	kg/m	-8.8498	-8.8498	-7.3592
Y_{uv_f}	kg/m	-15.0442	-15.0351	-13.7738
Y_{uv}	kg/m	-23.8940	-23.8849	-21.1329
$Y_{\|v\|v_b}$	kg/m	-48.5246	-53.6286	-47.7532
$Y_{\|v\|v_f}$	kg/m	-5.3518	-5.4066	-5.1899
$Y_{\|v\|v}$	kg/m	-53.8764	-59.0353	-52.9431
$Y_{\dot{r}_b}$	$kg \cdot m/rad$	0.0000	-0.2194	0.0127
$Y_{\dot{r}_f}$	$kg \cdot m/rad$	0.1132	0.1154	0.1458
$Y_{\dot{r}}$	$kg \cdot m/rad$	0.1132	-0.1040	0.1585
N_{uv_b}	kg	1.1039	1.1039	3.1058
N_{uv_f}	kg	5.1677	5.1646	5.5997
N_{uv}	kg	6.2716	6.2685	8.7056
$N_{\|v\|v_b}$	kg	0.0000	-1.1366	0.0921
$N_{\|v\|v_f}$	kg	1.8433	1.8662	1.8380
$N_{\|v\|v}$	kg	1.8433	0.7296	1.9301

Table 3.3: Coefficients obtained from yaw maneuver

Coefficient	Units	Prolate Spheroid	Myring Profile	SATLP
$N_{\dot{r}_b}$	$kg \cdot m^2/rad$	-0.1877	-0.3280	-0.2484
$N_{\dot{r}_f}$	$kg \cdot m^2/rad$	-0.0389	-0.0397	-0.0547
$N_{\dot{r}}$	$kg \cdot m^2/rad$	-0.2266	-0.3676	-0.3031
$N_{\|r\|r_b}$	$kg \cdot m^2/rad^2$	-0.5922	-0.6942	-0.5617
$N_{\|r\|r_f}$	$kg \cdot m^2/rad^2$	-0.2204	-0.2130	-0.0985
$N_{\|r\|r}$	$kg \cdot m^2/rad^2$	-0.8126	-0.9072	-0.6602
N_{ur_b}	$kg \cdot m/rad$	0.0000	0.0000	-0.9467
N_{ur_f}	$kg \cdot m/rad$	-1.7751	-1.7740	-1.9256
N_{ur}	$kg \cdot m/rad$	-1.7751	-1.7740	-2.8723
$Y_{\|r\|r_b}$	$kg \cdot m/rad^2$	0.0000	-0.3981	0.3701
$Y_{\|r\|r_f}$	$kg \cdot m/rad^2$	0.6365	0.6459	0.2395
$Y_{\|r\|r}$	$kg \cdot m/rad^2$	0.6365	0.2478	0.6096
Y_{ur_b}	kg/rad	0.0000	0.0000	2.8976
Y_{ur_f}	kg/rad	5.1677	5.1646	5.0462
Y_{ur}	kg/rad	5.1677	5.1646	7.9439

the yaw maneuver. For the sway maneuver, the measured net lateral force on the SATLP is in satisfactory agreement with the predictions of the ASE coefficients for the prolate spheroid and Myring profile. However, for the net yaw-axis moment, The prolate spheroid approximation yields significantly better agreement than the Myring profile. For the yaw maneuvers satisfactory agreement is seen for both the lateral force and yaw-axis moment. Furthermore, there is no considerable difference between the predictions of the Myring profile and prolate spheroid

Given the significant prediction error seen in the yaw-axis moment of the sway maneuver by the Myring profile, the preferred method of approximation is the prolate spheroid.

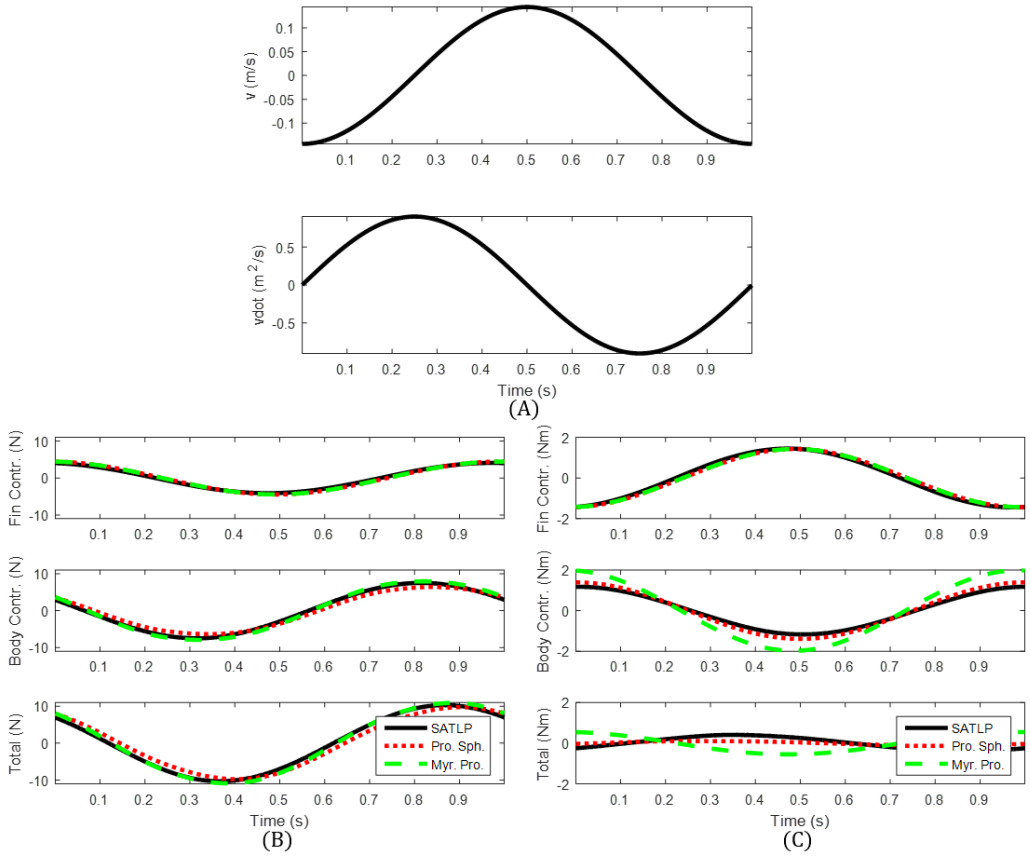

Figure 3.9: VPMM sway study of the tail controlled SATLP, prolate spheroid, and Myring Profile. (A) Prescribed motion trajectories, (B) Lateral force, (C) Yaw-axis moment

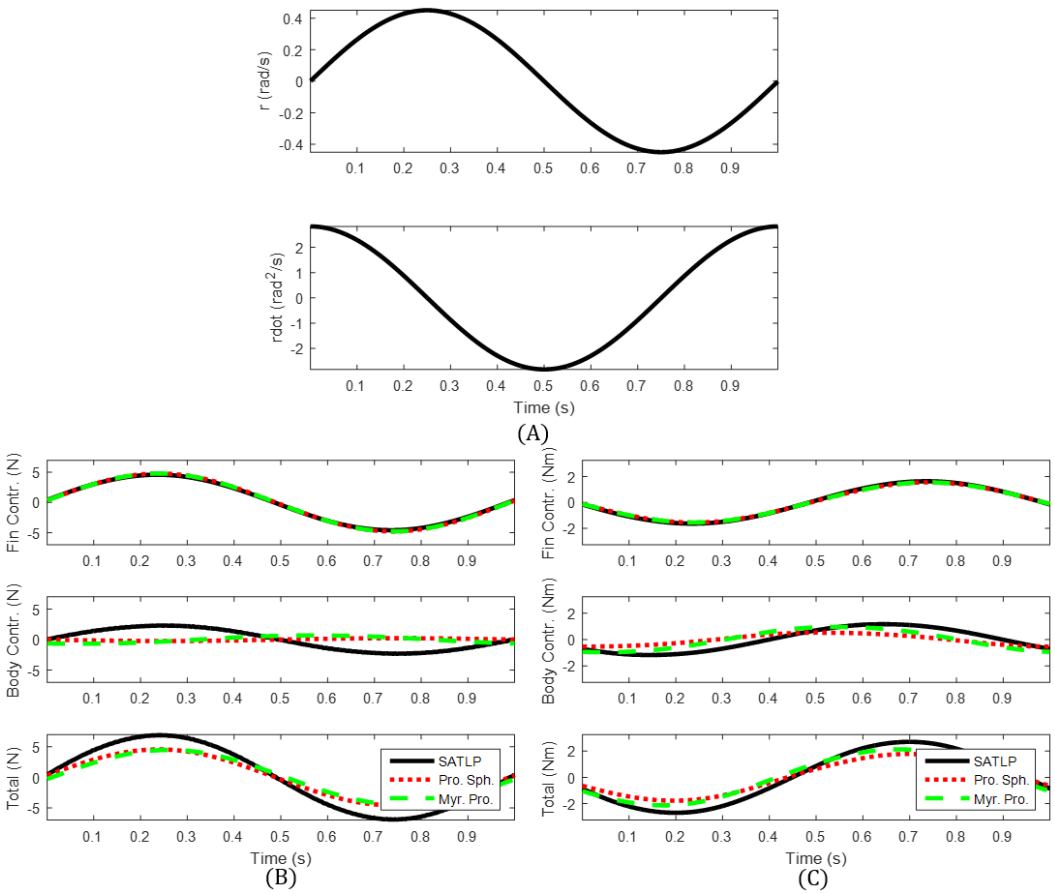

Figure 3.10: VPMM yaw study of the tail controlled SATLP, prolate spheroid, and Myring Profile. (A) Prescribed motion trajectories, (B) Lateral force, (C) Yaw-axis moment

The satisfactory agreement seen in these studies suggest that it is appropriate for the coefficients obtained from the methods in Chapter 2 to serve as a preliminary approximation of the vehicle's dynamic behavior. In turn, as the vehicle design becomes finalized, captive tests should be physically conducted or simulated to obtain the vehicle's final set of coefficients.

3.3 SATLP Parameter Identification

The final design of the SATLP vehicle consists of control surfaces placed at the nose, along with a ducted propeller, as seen in Figure 3.11. Hydrodynamic coefficients for the SATLP

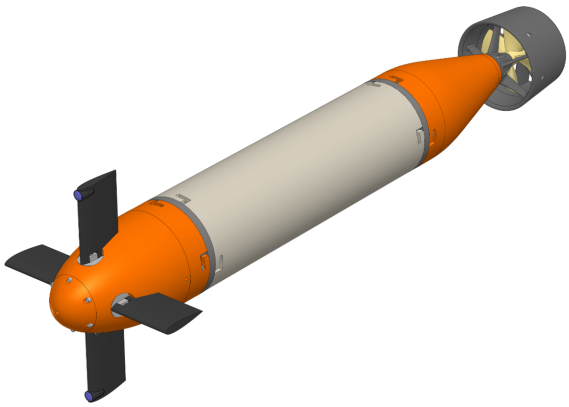

Figure 3.11: Final design of the nose-finned SATLP vehicle

vehicle have been estimated from the surge, sway, and yaw VPMM trials using the approach described in Section 3.1. The coefficients appear in Table B.1 in Appendix B.

In Figure 3.12, the measured forces and moments are overlaid by the force and moment calculated using the identified coefficients. Satisfactory agreement is seen amongst the trajectories. These resulting coefficients will be the vehicle's final set of coefficients used for controller design and simulation.

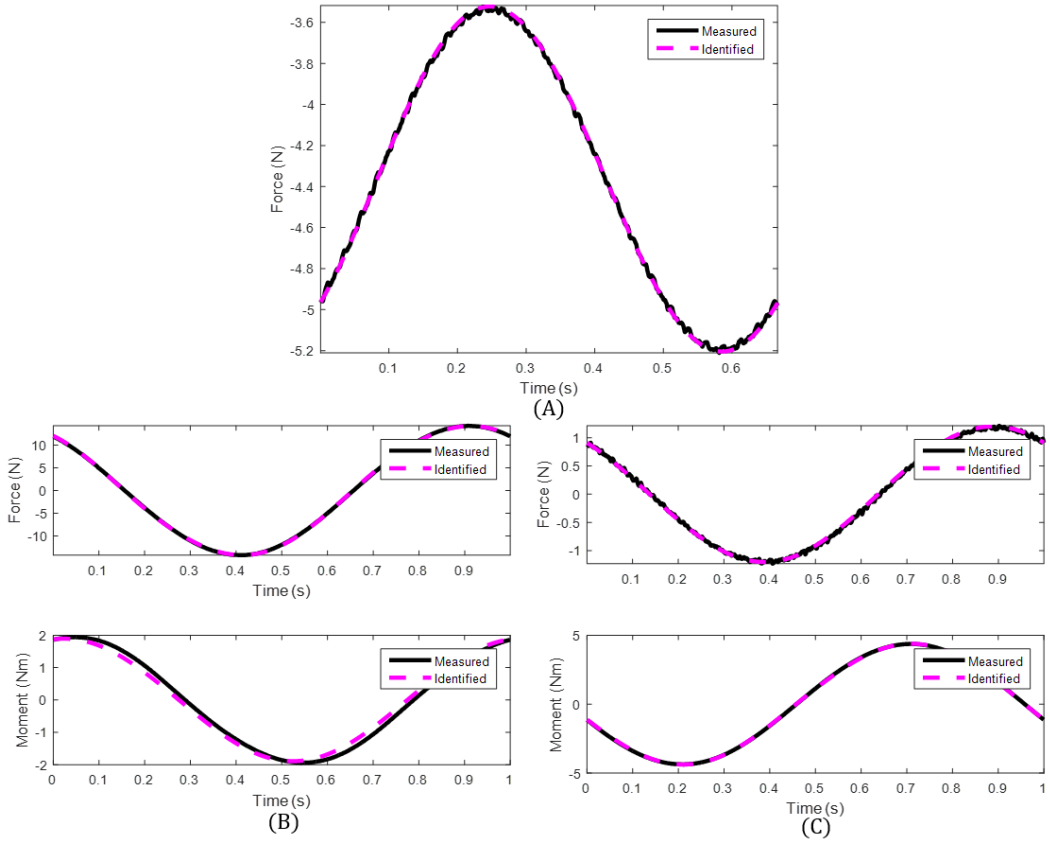

Figure 3.12: Verification of parameter estimation for the SATLP vehicle. (A) Surge Manuever, (B) Sway Maneuver, (C) Yaw Maneuver

Chapter 4

Rope Model

To model the dynamic behavior of the rope, the rope is approximated by a system of lumped mass-spring-damper models, similar to the formulation presented by Huang in [16]. The lumped mass-spring-damper approximation spatially discretizes the rope into N massless links, connected by spherical frictionless joints. With the lumped mass approach, the mass of each joint is the average mass of its adjacent links. Likewise, the external forces acting on a joint are the average of the external forces acting on the adjacent links.

The links consist of extensible spring-damper elements. Hence, the link internal constraint forces are easily computed from spring and damper forces. The spring-damper modeling approach is considered advantageous to rope dynamic models where the links are rigid since the rigidity requires an internal constraint force for each link to be calculated by solving a linear set of algebraic equations [33].

Lagrangian mechanics have been used as an alternative to the lumped-mass approach to derive the equations of motion for a rope system. Formulations of multi-rigid-body dynamic models using Lagrangian mechanics can be found in [18] and the sources cited therein.

In contrast to Lagrangian methods, the lumped mass spring-damper method preserves the physical interpretation of the forces acting on the rope, facilitating coupling of the vehicle and rope models. Additionally, as the angular orientation of the link changes relative to the fluid flow, the added mass matrix associated with the link varies. Capturing this phenomenon

is critical for modeling the transient behavior of when a vehicle enters or exits a turn. As compared to Lagrangian mechanics, the lumped mass spring-damper method is much better suited to appropriately model this effect.

With the exception of [4], the existing literature prescribes the motion of the tow point. Inherent with this approach is the assumption that the forces and moments imparted by the rope on the vehicle are considered negligible relative to all other external forces acting on the vehicle. This is true for vessels whose mass is orders of magnitude greater than that of the payload, however for vehicles towing a payload of comparable or even greater size, the coupling between the vehicle and rope dynamics must be accurately captured. The rope dynamic model derived in this chapter accomplishes this objective.

4.1 Kinematics

The configuration of the AUV-Rope system is depicted in Figure 4.1. A reference frame $\mathcal{F}_k$

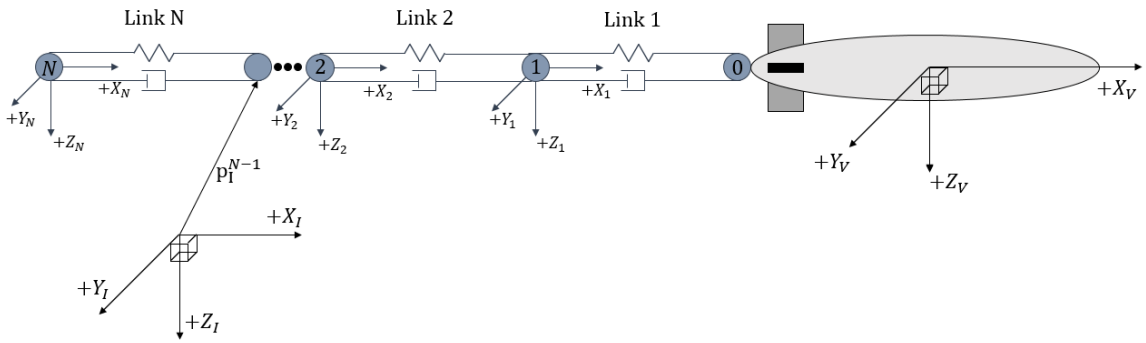

Figure 4.1: AUV-Rope system configuration

is attached to link k, $1 \leq k \leq N$. The origin of $\mathcal{F}_k$ is located at the k^{th} joint, whose inertial

position is specified by the vector

$$\mathrm{p}_I^k = \left[x_I^k,\ y_I^k,\ z_I^k \right]^{\mathsf{T}}, \tag{4.1}$$

The orientation of $\mathcal{F}_k$ with respect to $\mathcal{F}_I$ is specified using the Euler angles θ^k and ψ^k, denoting the pitch and yaw angle, respectively. The torsion of the link is not considered, thus the yaw and pitch angles are sufficient to specify the link orientation in $\mathcal{F}_I$. The definitions and sign convention for the Euler angles are illustrated in Figure 4.2.

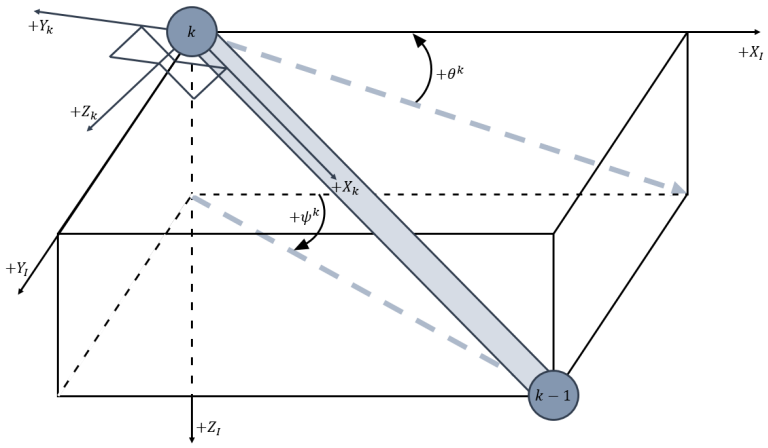

Figure 4.2: Definitions and sign convention for the Euler angles of the k^{th} link

To transform local link coordinates to inertial coordinates, a (ZYX) rotation sequence is employed, yielding the rotation matrix

$$R_{Ik} = \begin{bmatrix} \cos(\psi^k)\cos(\theta^k) & -\sin(\psi^k) & \cos(\psi^k)\sin(\theta^k) \\ \sin(\psi^k)\cos(\theta^k) & \cos(\psi^k) & \sin(\theta^k)\sin(\psi^k) \\ -\sin(\theta^k) & 0 & \cos(\theta^k) \end{bmatrix}. \tag{4.2}$$

Note that the rotation matrix R_{Ik} can be obtained by substituting the link Euler angles in

(2.4) with $\phi^k = 0$. Thus, the velocity of the k^{th} joint expressed in the inertial frame is

$$\dot{\mathrm{p}}_I^k = \mathrm{v}_I^k = R_{Ik}\mathrm{v}_k^k, \tag{4.3}$$

where v_k^k represents the velocity of the k^{th} joint expressed in $\mathcal{F}_k$. The inverse relationship is given by

$$\mathrm{v}_k^k = (R_{Ik})^{-1}\mathrm{v}_I^k, \tag{4.4}$$

with $R_{kI} = (R_{Ik})^{-1} = (R_{Ik})^{\mathsf{T}}$. Given that the local $+X$ axis extends along the length of the of each link, the only non-zero component, with respect to the local link frame, is along the tangential direction, resulting in the following relationship for the k^{th} link

$$\begin{bmatrix} (x_I^{k-1} - x_I^k) \\ (y_I^{k-1} - y_I^k) \\ (z_I^{k-1} - z_I^k) \end{bmatrix} = R_{Ik} \begin{bmatrix} l^k \\ 0 \\ 0 \end{bmatrix}, \tag{4.5}$$

where the length of the k^{th} link is

$$l^k = \sqrt{(x_I^{k-1} - x_I^k)^2 + (y_I^{k-1} - y_I^k)^2 + (z_I^{k-1} - z_I^k)^2}. \tag{4.6}$$

For the case when $k = 1$, the upper boundary condition for the link is given by the inertial position of the vehicle tow attachment point, that is

$$\begin{bmatrix} x_I^{k-1} \\ y_I^{k-1} \\ z_I^{k-1} \end{bmatrix} = \begin{bmatrix} x_I^t \\ y_I^t \\ z_I^t \end{bmatrix}. \tag{4.7}$$

Decomposing (4.5) yields a system of equations to solve for the link Euler angles

$$(x_I^{k-1} - x_I^k) = l^k \cos(\theta^k) \cos(\psi^k) \tag{4.8}$$

$$(y_I^{k-1} - y_I^k) = l^k \cos(\theta^k) \sin(\psi^k) \tag{4.9}$$

$$(z_I^{k-1} - z_I^k) = -l^k \sin(\theta^k). \tag{4.10}$$

From (4.10) the pitch angle is calculated as

$$\theta^k = \sin^{-1}\left(\frac{(z_I^{k-1} - z_I^k)}{-l^k}\right). \tag{4.11}$$

The equation to calculate the yaw angle ψ^k is obtained by solving (4.8) and (4.9) for $\cos(\theta^k)$ and equating the two results

$$\psi^k = \text{atan2}\Big((y_I^{k-1} - y_I^k), (x_I^{k-1} - x_I^k)\Big), \tag{4.12}$$

where the function $\text{atan2}(\text{y}, \text{x})$ is defined as

$$\text{atan2}(\text{y}, \text{x}) = \begin{cases} \tan^{-1}(\frac{\text{y}}{\text{x}}) & x > 0, \\ \tan^{-1}(\frac{\text{y}}{\text{x}}) + \pi & x < 0 \text{ and } y \geq 0, \\ \tan^{-1}(\frac{\text{y}}{\text{x}}) - \pi & x < 0 \text{ and } y < 0, \\ \pi/2 & x = 0 \text{ and } y > 0, \\ -\pi/2 & x = 0 \text{ and } y < 0, \\ \text{undefined} & x = 0 \text{ and } y = 0. \end{cases} \tag{4.13}$$

The function atan2(·) is used to preserve the appropriate quadrant. It is worth noting, atan2(·) is undefined when $(y_I^{k-1} - y_I^k) = (x_I^{k-1} - x_I^k) = 0$. This condition arises when the

link is completely vertical. This situation will not arise for the application at hand, given that the positively buoyant rope will have a tendency to lie along the surface of the water. For other applications in which this scenario is likely to occur, modeling of mooring cable dynamics for example, the reference frame and orientation angles must be defined using an appropriate convention. An example of a suitable convention can be found in [4].

4.2 Link Mass Matrix

The lumped mass contribution from the k^{th} link will consist of a component due to the dry mass m^k of the link, as well as a component due the added mass e^k of the link, calculated as

$$m^k = \rho_l \nabla^k \tag{4.14}$$

$$e^k = \rho \nabla^k. \tag{4.15}$$

The density of the fluid and link is denoted by ρ and ρ_l, respectively. The volume of the link with radius r_l is calculated as $\nabla^k = \pi r_l^2 l^k$.

With respect to the local link frame $\mathcal{F}_k$, the tangential added mass effect is considered negligible compared to the normal and bi-normal added mass effects. Thus the mass matrix of the k^{th} link is

$$M_k^k = \begin{bmatrix} m^k & 0 & 0 \\ 0 & m^k & 0 \\ 0 & 0 & m^k \end{bmatrix} + \begin{bmatrix} 0 & 0 & 0 \\ 0 & e^k & 0 \\ 0 & 0 & e^k \end{bmatrix}. \tag{4.16}$$

To obtain the mass matrix with respect to $\mathcal{F}_I$, the mass matrix transformation is applied

$$M_I^k = R_{Ik} M_k^k (R_{Ik})^\mathsf{T}. \tag{4.17}$$

Similar formulations of the link mass matrix appear in [4, 34].

4.3 Link Forces

This section presents the formulation of the internal and external forces for each link. The forces are derived with respect to the local link frame, and then transformed into the inertial frame.

4.3.1 Internal Forces

Approximating the behavior of the rope using a mass-spring-damper system models the internal constraint forces as the sum of a tension force and an internal damping force. These formulations are adopted from those presented by Huang in [16]. The tension force acts solely along the length of the link, and is modeled using Hooke's Law, such that the local link tension force vector is

$$T_k^k = \begin{bmatrix} EA\frac{l^k - l_u}{l_u}, & 0, & 0 \end{bmatrix}^\mathsf{T} \tag{4.18}$$

where A and l_u denote the cross sectional area and the unstretched length of the link, respectively. The effective Young's modulus E characterizes the axial stiffness of the rope.

The friction among the stranded braids of the rope generates a damping effect, and analogous to the tension force, the damping force acts along the length of the link. The force is assumed

to be directly proportional with the axial strain rate, such that the local link damping force vector is

$$P_k^k = \begin{bmatrix} C_v(\dot{x}_k^{k-1} - \dot{x}_k^k), & 0, & 0 \end{bmatrix}^{\mathsf{T}}, \tag{4.19}$$

where C_v is the internal viscous damping coefficient. The tangential velocity, with respect to $\mathcal{F}_k$, of the upper joint is denoted by $\dot{x}_k^{k-1}$, which is

$$\begin{bmatrix} \dot{x}_k^{k-1} \\ \dot{y}_k^{k-1} \\ \dot{z}_k^{k-1} \end{bmatrix} = R_{kI} \begin{bmatrix} \dot{x}_I^{k-1} \\ \dot{y}_I^{k-1} \\ \dot{z}_I^{k-1} \end{bmatrix}. \tag{4.20}$$

Lastly, to express the local link forces in the inertial frame, the following rotations are employed

$$T_I^k = R_{Ik} T_k^k, \qquad\qquad P_I^k = R_{Ik} P_k^k. \tag{4.21}$$

4.3.2 External Forces

The external forces acting on each link include fluid drag forces, and restorative forces due to gravity and buoyancy.

Fluid Drag

The fluid drag acting on each link is a function of the velocity of the centroid of the link, interpolated by averaging the velocities of the link's bounding joints

$$\bar{\mathrm{v}}_I^k = \frac{1}{2}(\mathrm{v}_I^{k-1} + \mathrm{v}_I^k). \tag{4.22}$$

From [22], the local link fluid drag is modeled empirically as

$$D_k^k = -\frac{1}{2}\rho \begin{bmatrix} \pi d_l l^k C_t |\dot{\bar{x}}_k^k| \dot{\bar{x}}_k^k \\ d_l l^k C_n |\dot{\bar{y}}_k^k| \dot{\bar{y}}_k^k \\ d_l l^k C_n |\dot{\bar{z}}_k^k| \dot{\bar{z}}_k^k \end{bmatrix}. \tag{4.23}$$

The diameter of the link is d_l. For a submerged circular cylinder, Reid and Wilson [29] give the tangential drag coefficient

$$C_t = 2\frac{k}{\ln(\frac{120}{s/a})}, \tag{4.24}$$

where $k = 0.4$ is the von Karman constant, and s is the surface roughness diameter.

Experiments to determine the tangential drag coefficient of the rope were conducted at Claytor Lake in Dublin, Virginia. The rope was attached to a load cell to measure the drag force acting on the rope for various lengths as it was being towed from a boat at varying speeds. The experimental data is shown in Figure 4.3.

Reid and Wilson's formulation of the tangential drag coefficient is based on a fully submerged cylinder. Given the positively buoyant rope, the rope will have a tendency to rise to the surface, such that for sufficiently long lengths of rope, the tail end of the rope will be half submerged, and the other half will be exposed to the surface. In experimentally determining

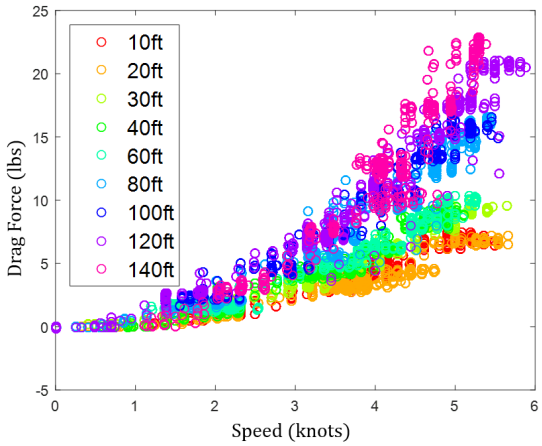

Figure 4.3: Experimental drag force for different length ropes at varying speeds

the drag coefficient of the rope, it is desirable to use data from when the rope is fully submerged so as to compare the experimental results to those obtained by Reid and Wilson.

The longest length for which the entire rope was submerged was 80 ft. Using the measured data in Figure 4.4, a regression to obtain the tangential drag coefficient was performed. Having obtained the coefficient, the fitted drag force is plotted along with the measured data. The regression yields a drag coefficient $C_t = 0.0102$. Using Reid and Wilson's formulation (4.24) with the surface roughness diameter $s = 2mm$ and a rope radius $a = 12mm$ yields the drag coefficient of $C_t = 0.00739$.

The experimental results over predict the drag coefficient offered by Reid and Wilson. This over prediction is due largely in part to the inability to mitigate the effects of crossflow drag acting on the slightly inclined buoyant rope.

Since the tangential drag could not be experimentally isolated from the crossflow drag, the tangential drag coefficient from Reid and Wilson is used for simulation purposes. The normal

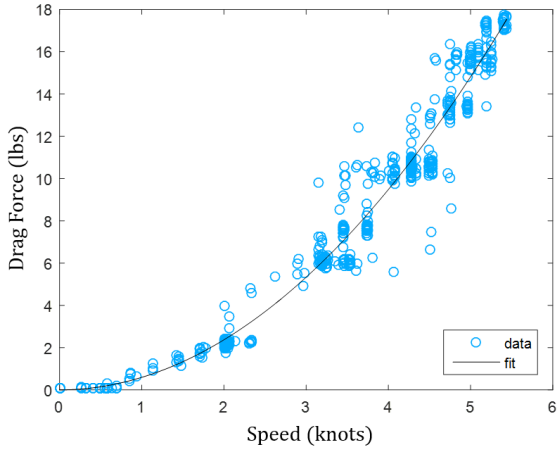

Figure 4.4: Experimental drag results for 80ft. of submerged rope

drag coefficient used for simulation purposes is that offered by Kamman in [22]

$$C_n = \begin{cases} 0 & Re_n \leq 0.1 \\ 0.45 + \frac{5.93}{(Re_n)^{0.33}} & 0.1 < Re_n \leq 400 \\ 1.27 & 400 < Re_n \leq 10^5 \\ 0.3 & 10^5 < Re_n \end{cases}, \tag{4.25}$$

where the Reynold's number for the normal component of the link velocity is defined

$$Re_n = \frac{\rho d_l |\dot{\tilde{y}}_L^k|}{\mu}, \tag{4.26}$$

with μ denoting dynamic viscosity of the fluid. For water at 20°C., the dynamic viscosity is $\mu = 1.002 mPa \cdot s$.

Restorative Forces

The restorative forces acting on an individual link are due to gravity and buoyancy. With respect to the inertial frame, the gravitational and buoyant forces are given by

$$G_I^k = \begin{bmatrix} 0, & 0, & \rho_l \nabla^k g \end{bmatrix}^\mathsf{T}, \qquad B_I^k = \begin{bmatrix} 0, & 0, & -\rho \nabla^k g \end{bmatrix}^\mathsf{T}. \tag{4.27}$$

The accleration due to gravity is $9.81 m/s^2$, where the positive acceleration is in the direction of the $+Z_I$ axis.

4.4 Equations of Motion

Given that the rope dynamics evolve with respect to the inertial frame, the position of each joint is obtained by directly integrating inertial velocities.

The dynamic equations of motion describe the evolution of the rope system due to the forces acting on it. For the lumped mass approximation, the mass of each joint is the average mass of the adjacent links. Likewise, the external forces acting on the link are the average of the external forces acting on the adjacent links such that the dynamics of the k^{th} joint are

$$\begin{aligned} \frac{1}{2}(M_I^k + M_I^{k+1})\ddot{\mathrm{p}}_I^k =& (T_I^k - T_V^{k+1}) + (P_I^k - P_I^{k+1}) \\ &+ \frac{1}{2}(D_I^k + D_I^{k+1}) + \frac{1}{2}(G_I^k + G_I^{k+1}) + \frac{1}{2}(B_I^k + B_I^{k+1}). \end{aligned} \tag{4.28}$$

The forces acting on the k^{th} node are depicted in Figure 4.5. The dynamics (4.28) apply for joints $k \in [1, N-1]$, The last joint, however, has only the preceding link as an adjacent link,

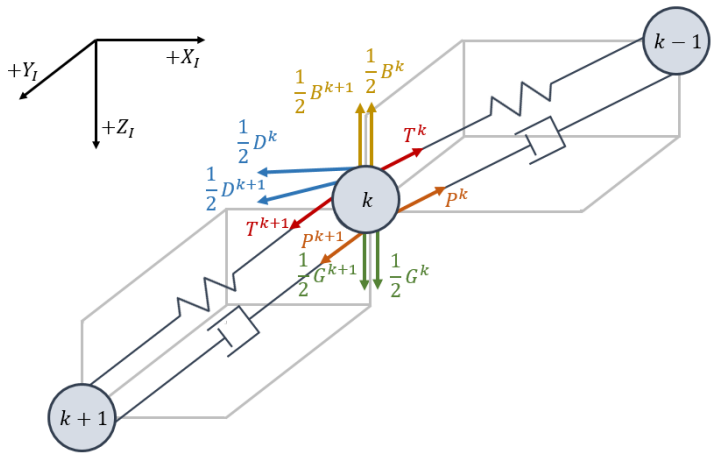

Figure 4.5: Summation of forces acting on the k^{th} joint

thus the dynamics for the N^{th} joint are given by

$$M_I^N \ddot{\mathrm{p}}_I^N = T_I^N + P_I^N + \frac{1}{2}(D_I^N + G_I^k + B_I^k). \tag{4.29}$$

4.5 Forces and Moments Acting on the Vehicle

The forces acting on the vehicle are obtained by treating the towing attachment point on the vehicle as the 0^{th} joint. With this consideration, the rope force acting on the vehicle is

$$f_V^R = R_{VI}^{\eta_1}[-T_I^1 - P_I^1 + \frac{1}{2}(D_I^1 + G_I^1 + B_I^1)]. \tag{4.30}$$

Thus the vector containing the force and moment acting on the vehicle from the rope is

$$F_V^R = \begin{bmatrix} f_V^R \\ \mathrm{p}_V^t \times f_V^R \end{bmatrix}, \tag{4.31}$$

where $\mathrm{p}_V^t = \begin{bmatrix} x_V^t, & y_V^t, & z_V^t \end{bmatrix}^\mathsf{T}$ denotes the position of the tow attachment point, with respect to the vehicle-fixed frame.

Chapter 5

Assessment of Proportional Steering Control

Conventional control methodologies for streamline underwater vehicles assume the vehicle's dynamics can be partitioned into three noninteracting (or lightly interacting) subsystems for steering, diving, and speed. For the Naval Postgraduate School (NPS) AUV II, Healey and Marco developed proportional-integral-derivative (PID) feedback controllers for each subsystem and achieved satisfactory performance [13]. More advanced nonlinear control techniques, such as sliding mode control, have been successfully employed and implemented on AUVs like the Norwegian Defense Research Establishment (NDRE) AUV as reported by Jalving in [21]. The assumption of non-interacting subsystems has also been applied for naval submarines. Successful application of a decoupled depth controller using H_∞ techniques has been demonstrated by Marshfield for a standard submarine in [25].

Invoking the assumption of non-interacting subsystems for the vehicle-payload system, preliminary control analysis is presented, assessing solely the performance of a steering autopilot for heading control.

5.1 Steering Equations of Motion

The steering equations of motion of the vehicle-rope system are obtained by constraining the local vehicle velocities, such that $w = p = q = 0$, and the rope joints such that $z_I^k = \dot{z}_I^k = 0 \; \forall \; k \; \in [1, N]$. Hence, the state vector of the system reduces to

$$\mathrm{x} = \left[\mathrm{p}^\mathsf{T}, \; \mathrm{v}^\mathsf{T} \right]^\mathsf{T}, \tag{5.1}$$

where the vectors

$$\mathrm{p} = [\overbrace{x_I, \; y_I, \; \psi}^{\eta^\mathsf{T}}, \overbrace{x_I^1, \; y_I^1}^{(\mathrm{p}_I^1)^\mathsf{T}}, \; \cdots, \; \overbrace{x_I^N, \; y_I^N}^{(\mathrm{p}_I^N)^\mathsf{T}}]^\mathsf{T},$$
$$\mathrm{v} = [\overbrace{u, \; v, \; \; r}^{\nu^\mathsf{T}}, \overbrace{\dot{x}_I^1, \; \dot{y}_I^1}^{(\mathrm{v}_I^1)^\mathsf{T}}, \; \cdots, \; \overbrace{\dot{x}_I^N, \; \dot{y}_I^N}^{(\mathrm{v}_I^N)^\mathsf{T}}]^\mathsf{T},$$

contain the positions and velocities, respectively, of the vehicle and link joints.

The equations of motion for the vehicle-rope system are

$$\dot{\mathrm{x}} = \begin{bmatrix} \dot{\eta} \\ \dot{\mathrm{p}}_I^1 \\ \dot{\mathrm{p}}_I^2 \\ \vdots \\ \dot{\mathrm{p}}_I^{N-1} \\ \dot{\mathrm{p}}_I^N \\ \dot{\nu} \\ \dot{\mathrm{v}}_I^1 \\ \dot{\mathrm{v}}_I^2 \\ \vdots \\ \dot{\mathrm{v}}_I^{N-1} \\ \dot{\mathrm{v}}_I^N \end{bmatrix} = \begin{bmatrix} R_{IV}\nu \\ \mathrm{v}_I^1 \\ \mathrm{v}_I^2 \\ \vdots \\ \mathrm{v}_I^{N-1} \\ \mathrm{v}_I^N \\ (M_V)^{-1}[-C_V(\nu)\nu + D_V(\nu)\nu + \tau_V^C + \tau_V^R] \\ \frac{1}{2}(M_I^1 + M_I^2)^{-1}[T_I^1 - T_I^2 + P_I^1 - P_I^2 + \frac{1}{2}(D_I^1 + D_I^2)] \\ \frac{1}{2}(M_I^2 + M_I^3)^{-1}[T_I^2 - T_I^3 + P_I^2 - P_I^3 + \frac{1}{2}(D_I^2 + D_I^3)] \\ \vdots \\ \frac{1}{2}(M_I^{N-1} + M_I^N)^{-1}[T_I^{N-1} - T_I^N + P_I^{N-1} - P_I^N + \frac{1}{2}(D_I^{N-1} + D_I^N)] \\ (M_I^N)^{-1}[T_I^N + P_I^N + \frac{1}{2}D_I^N] \end{bmatrix}. \quad (5.2)$$

For the local vehicle dynamics, the truncated matrices are

$$M_V = \begin{bmatrix} m_v - X_{\dot{u}} & 0 & 0 \\ 0 & m_v - Y_{\dot{v}} & -Y_{\dot{r}} \\ 0 & -Y_{\dot{r}} & J_z - N_{\dot{r}} \end{bmatrix}, \quad C_V(\nu) = \begin{bmatrix} 0 & 0 & -m_v v + (Y_{\dot{v}} v + Y_{\dot{r}} r) \\ 0 & 0 & m_v u - X_{\dot{u}} u \\ m_v v - (Y_{\dot{v}} v + Y_{\dot{r}} r) & -m_v u + X_{\dot{u}} u & 0 \end{bmatrix},$$

$$D_V(\nu) = \begin{bmatrix} X_{|u|u}|u| & 0 & 0 \\ 0 & Y_{|v|v}|v| + Y_{uv}u & Y_{|r|r}|r| + Y_{ur}u \\ 0 & N_{|v|v}|v| + N_{uv}u & N_{|r|r}|r| + N_{ur}u \end{bmatrix}, \qquad \tau_V^C = \begin{bmatrix} X_{prop} \\ Y_{uu\delta_r} u^2 \delta_r \\ N_{uu\delta_r} u^2 \delta_r \end{bmatrix}.$$

The forces and moment imparted on the vehicle from the rope, expressed in the vehicle

frame, are

$$\tau_V^R = \begin{bmatrix} f_{V,x}^R \\ f_{V,y}^R \\ f_{V,y}^R \cdot x_V^t \end{bmatrix}, \qquad \begin{bmatrix} f_{V,x}^R \\ f_{V,y}^R \end{bmatrix} = R_{VI}^{\eta_1}(-T_I^1 - P_I^1 + \frac{1}{2}D_I^1).$$

The transformation matrix

$$R_{IV} = \begin{bmatrix} R_{IV}^{\eta_1} & 0_{2\times 1} \\ 0_{1\times 2} & 1 \end{bmatrix} = \begin{bmatrix} \cos(\psi) & -\sin(\psi) & 0 \\ \sin(\psi) & \cos(\psi) & 0 \\ 0 & 0 & 1 \end{bmatrix}, \tag{5.3}$$

is used to express the local vehicle velocities in the inertial frame. Descriptions of the parameters and methods to obtain the coefficients that govern the vehicle dynamics are detailed in Chapter 2.

The mass matrix for the k^{th} link expressed in the local link frame $\mathcal{F}_k$ is

$$M_k^k = \begin{bmatrix} m^k & 0 \\ 0 & m^k \end{bmatrix} + \begin{bmatrix} 0 & 0 \\ 0 & e^k \end{bmatrix}, \tag{5.4}$$

where the dry and added mass of the link are denoted by m_l^k and e_l^k, respectively. The local internal and external forces of the k^{th} link reduce to

$$T_k^k = \begin{bmatrix} EA\frac{l^k - l_u}{l_u} \\ 0 \end{bmatrix}, \quad P_k^k = \begin{bmatrix} C_v(\dot{x}_k^{k-1} - \dot{x}_k^k) \\ 0 \end{bmatrix}, \quad D_k^k = -\frac{1}{2}\rho \begin{bmatrix} \pi d_l l^k C_t |\dot{\bar{x}}_k^k| \dot{\bar{x}}_k^k \\ d_l l^k C_n |\dot{\bar{y}}_k^k| \dot{\bar{y}}_k^k \end{bmatrix}. \tag{5.5}$$

The orientation of the k^{th} link is calculated using the positions of the bounding joints

$$\psi^k = \text{atan2}\big((y_I^{k-1} - y_I^k), (x_I^{k-1} - x_I^k)\big). \tag{5.6}$$

Using the rotation matrix

$$R_{Ik} = \begin{bmatrix} \cos(\psi^k) & -\sin(\psi^k) \\ \sin(\psi^k) & \cos(\psi^k) \end{bmatrix}, \tag{5.7}$$

the mass matrix and the forces associated with the k^{th} link are expressed in the inertial frame by applying the transformation

$$M_I^k = R_{Ik} M_k^k (R_{Ik})^{-1}, \tag{5.8}$$

$$T_I^k = R_{Ik} T_k^k, \tag{5.9}$$

$$P_I^k = R_{Ik} P_k^k, \tag{5.10}$$

$$D_I^k = R_{Ik} D_k^k. \tag{5.11}$$

Descriptions of the parameters governing the rope dynamics are detailed in Chapter 4.

5.2 Proportional Feedback Control Law

The SATLP vehicle is instrumented with an attitude and heading reference system (AHRS) to measure the vehicle's inertial heading angle. The hydrophone sensors, placed on the edge of the control surfaces, measure the relative bearing of the vehicle to the target location. Based on the inertial and relative heading measurements, the onboard guidance system generates the desired heading angle $\psi_d(t)$ for the vehicle to intercept the target location.

For the vehicle to track the desired heading, the tracking error is introduced as $e(t) = \psi(t) - \psi_d(t)$. To regulate the heading error to zero, the proportional feedback control law is defined

$$\delta_r(t) = k_p e(t), \tag{5.12}$$

where $\delta_r(t)$ is the input rudder deflection angle. The proportional gain k_p is regarded as a design parameter that is tuned through a process of trial and error to achieve the desired tracking performance.

For sufficiently large angles of attack, the control surfaces experience nonlinear stall effects, violating the linear approximation of lift force. Consequently, the control law must be saturated such that the following inequality is satisfied

$$|\beta_e| = |\beta_f - \delta_r| < \bar{\beta}, \tag{5.13}$$

where $\bar{\beta}$ represents the angle of attack at which nonlinear stall effects begin to occur. For control surfaces with the assumed geometry of a NACA 0009 profile, the data given in [1] suggest using a limit of $\bar{\beta} = 12\ deg$. Since sway velocity is not measured, the angle β_f is not accessible. Informative estimates of β_f can be predicted by iteratively simulating predetermined maneuvers with the initialized saturated control law

$$\delta_r = \begin{cases} \delta_r, & |\delta_r| \leq \bar{\beta}, \\ \text{sgn}(\delta_r)\bar{\beta}, & |\delta_r| > \bar{\beta}, \end{cases} \tag{5.14}$$

observing β_f, and refining the control law to be

$$\delta_r = \begin{cases} \beta_f - \bar{\beta}, & \delta_r < \beta_f - \bar{\beta}, \\ \delta_r, & \beta_f - \bar{\beta} \leq \delta_r \leq \beta_f + \bar{\beta}, \\ \beta_f + \bar{\beta}, & \delta_r > \beta_f + \bar{\beta}. \end{cases} \tag{5.15}$$

This iterative update of β_f should be performed until $|\beta_f - \delta_r| < \bar{\beta}$ is satisfied for the entire simulation. However in most practical applications, the control law (5.14) yields satisfactory results and is implemented for simplicity.

5.3 System Simulation

Table 5.1: Size comparison of rope and SATLP vehicle

Description	Units	Vehicle	Rope
Total dry mass	kg	8.4335	16.2170
Length	m	0.8316	50.0000
Diameter	m	0.1238	0.0240

Using MATLAB's ordinary differential equation solver *ode*45, the dynamics of the SATLP-rope system were simulated. The rope used in the simulation was discretized into 50 links, and is modeled to be 1 $in.$ in diameter and 50 $m.$ in length. See Table 5.1 for a size comparison of the rope and vehicle. The value of proportional feedback controller gain is $k_p = 5000$. The hydrodynamic coefficients for the vehicle are those identified from the measured VPMM data in Chapter 3. Figure 5.1 shows the simulated vehicle trajectory in the inertial frame, heading angle of the vehicle, and the control input rudder deflection angle. The vehicle tracks the 90° change in desired heading within 25 seconds. Moreover, the control input is saturated until the heading error is regulated to zero, signifying that this is the fastest

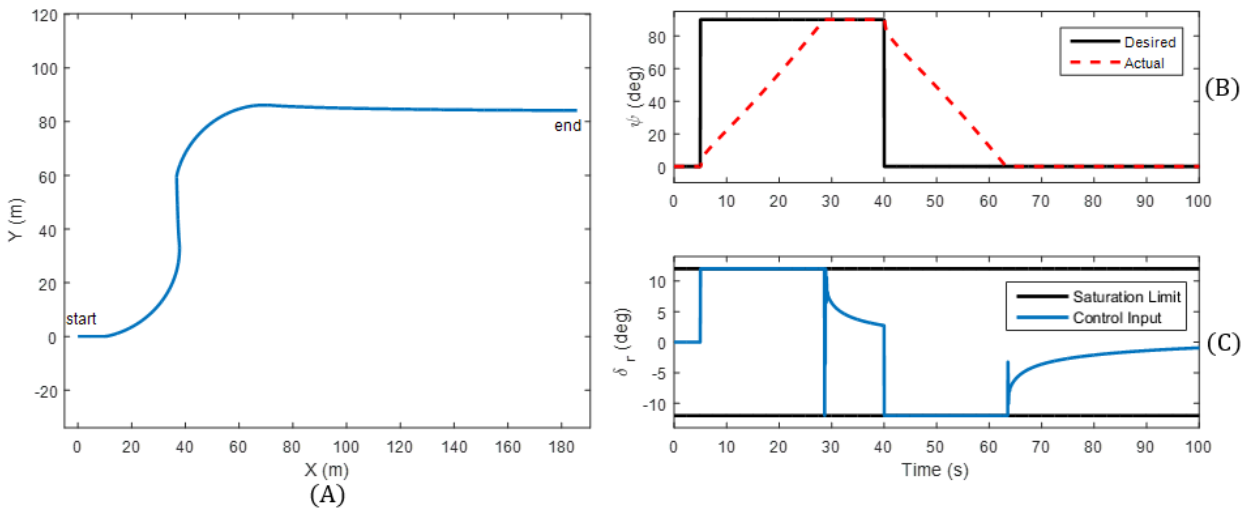

Figure 5.1: System simulation results.(A) Inertial vehicle trajectory, (B) Heading angle, (C) Control input

tracking response attainable for the vehicle.

The plots in Figure 5.2 show the links' angular displacements relative to the vehicle, along with the tension force within each link. During turning maneuvers, Link 1, which is attached directly to the vehicle, experiences the smallest angular displacement, while the largest displacement is experienced by the last link. The tension force acting on the first link is the largest, while the last link has the least amount of tension. Finally, upon transitioning from a turning maneuver to a straight line maneuver the angular displacements of the links converge to zero, relative to the vehcile. All of these simulated results are consistent with how a rope is expected to behave.

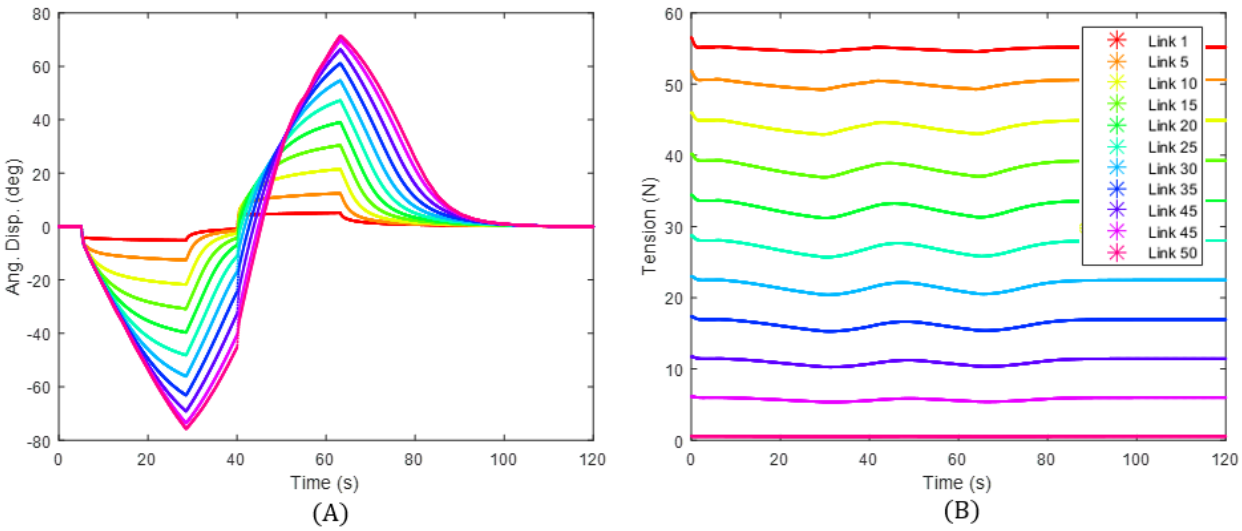

Figure 5.2: System simulation results. (A) Link displacement relative to vehicle, (B) Link tension force

Chapter 6

Conclusion

The agreement seen between the forces and moments predicted by ASE methods and those from CFD simulations suggests that it is appropriate to use ASE methods to estimate a vehicle's hydrodynamic coefficients. However, further studies should be conducted to see how the agreement of the net force and moment is affected as the size of the control surfaces is varied relative to the body. While the SATLP vehicle shows good agreement for the fin contributions, poor agreement is seen for the lateral force and yaw-axis moment acting on the body induced by rotary motion. As the control surface size decreases relative to the body, the agreement of the net forces and net moments may degrade. For sufficiently small control surfaces the analytic and semi-empirical methods may fail to yield satisfactory estimates of the vehicle's dynamic coefficients.

Simulation of the vehicle-payload system shows satisfactory tracking performance for heading control. A speed autopilot and a diving autopilot need to be designed and simulated for the vehicle-payload system. Furthermore, field trials need to be conducted to verify that the behavior of the closed system is consistent with the behavior predicted by the model.

Bibliography

[1] Ira H Abbott, Albert E Von Doenhoff, and Louis Stivers Jr. Summary of airfoil data. 1945.

[2] H. N. Arafat, D. J. Stilwell, and W. L. Neu. Development of a dynamic model of a small high-speed autonomous underwater vehicle. In *OCEANS 2006*, pages 1–6, Sept 2006. doi: 10.1109/OCEANS.2006.306895.

[3] Robert D Blevins. Applied fluid dynamics handbook. *New York, Van Nostrand Reinhold Co., 1984, 568 p.*, 1984.

[4] B Buckham, M Nahon, M Seto, X Zhao, and C Lambert. Dynamics and control of a towed underwater vehicle system, part i: model development. *Ocean Engineering*, 30 (4):453–470, 2003.

[5] J.P. Comstock. *Principles of Naval Architecture*. American Soc of Naval Architects and Marine Engineers, 1967. URL https://books.google.com/books?id=bFLVnQEACAAJ.

[6] EA De Barros, A Pascoal, and E De Sa. Investigation of a method for predicting auv derivatives. *Ocean Engineering*, 35(16):1627–1636, 2008.

[7] Bruno Ferreira, Miguel Pinto, Aníbal Matos, and Nuno Cruz. Hydrodynamic modeling and motion limits of auv mares. In *Industrial Electronics, 2009. IECON'09. 35th Annual Conference of IEEE*, pages 2241–2246. IEEE, 2009.

[8] Thor I. Fossen. *Guidance and control of ocean vehicles*. Wiley, Chichester; New York, 1994. ISBN 9780471941132; 0471941131.

[9] Thor I Fossen. *Handbook of marine craft hydrodynamics and motion control*. John Wiley & Sons, 2011.

[10] Morton Gertler. The dtmb planar-motion-mechanism system. Technical report, DAVID W TAYLOR NAVAL SHIP RESEARCH AND DEVELOPMENT CENTER BETHESDA MD DEPT OF HYDROMECHANICS, 1967.

[11] Morton Gertler and Grant R Hagen. Standard equations of motion for submarine simulation. Technical report, DAVID W TAYLOR NAVAL SHIP RESEARCH AND DEVELOPMENT CENTER BETHESDA MD, 1967.

[12] William Gracey. The additional-mass effect of plates as determined by experiments. 1941.

[13] Anthony J Healey, DB Marco, et al. Slow speed flight control of autonomous underwater vehicles: Experimental results with nps auv ii. In *The Second International Offshore and Polar Engineering Conference*. International Society of Offshore and Polar Engineers, 1992.

[14] Sighard F Hoerner. *Fluid-dynamic drag: practical information on aerodynamic drag and hydrodynamic resistance*. Hoerner Fluid Dynamics, 1965.

[15] Sighard F Hoerner and Henry V Borst. Fluid-dynamic lift, practical information on aerodynamic and hydrodynamic lift. Technical report, BORST (HENRY V) AND ASSOCIATES WAYNE PA, 1975.

[16] Shan Huang. Dynamic analysis of three-dimensional marine cables. *Ocean Engineering*, 21(6):587–605, 1994.

[17] DE Humphreys and KW Watkinson. Prediction of acceleration hydrodynamic coeffi-

cients for underwater vehicles from geometric parameters. Technical report, NAVAL COASTAL SYSTEMS LAB PANAMA CITY FL, 1978.

[18] Ronald L Huston, CE Passerello, and MW Harlow. Dynamics of multirigid-body systems. *Journal of applied Mechanics*, 45(4):889–894, 1978.

[19] Frederick H Imlay. The complete expressions for added mass of a rigid body moving in an ideal fluid. Technical report, DTIC Document, 1961.

[20] Petros A Ioannou and Jing Sun. *Robust adaptive control*, volume 1. PTR Prentice-Hall Upper Saddle River, NJ, 1996.

[21] Bjorn Jalving. The ndre-auv flight control system. *IEEE Journal of Oceanic Engineering*, 19(4):497–501, 1994.

[22] JW Kamman and TC Nguyen. A finite segment computer code to simulate the dynamics of towed cable systems. Technical report, NAVAL COASTAL SYSTEMS CENTER PANAMA CITY FL, 1990.

[23] Gustav Kirchhoff. Uber die bewegung eines rotationskorpers in einer flussigkeit. *Crelle J.*, pages 237–273, 1869.

[24] Horace Lamb. *Hydrodynamics*. Cambridge university press, 1932.

[25] WB Marshfield. Submarine periscope-depth depth-keeping using an h-infinity controller together with sea-noise-reduction notch filters. *Transactions of the Institute of Measurement and Control*, 13(5):233–240, 1991.

[26] DF Myring. A theoretical study of body drag in subcritical axisymmetric flow. *The Aeronautical Quarterly*, 27(3):186–194, 1976.

[27] JN Newman. Marine hydrodynamics. 1977.

[28] Timothy Jason Prestero. Verification of a six-degree of freedom simulation model for the remus autonomous underwater vehicle. Master's thesis, Massachusetts institute of technology, 2001.

[29] Robert O Reid and Basil W Wilson. Boundary flow along a circular cylinder. Technical report, TEXAS A AND M UNIV COLLEGE STATION, 1962.

[30] Sia Chuan Tang. *Modeling and simulation of the autonomous underwater vehicle, Autolycus*. PhD thesis, Massachusetts Institute of Technology, 1999.

[31] Sulin Tang, Tamaki Ura, Takeshi Nakatani, Blair Thornton, and Tao Jiang. Estimation of the hydrodynamic coefficients of the complex-shaped autonomous underwater vehicle tuna-sand. *Journal of marine science and technology*, 14(3):373–386, 2009.

[32] Michael S Triantafyllou and Franz S Hover. *Maneuvering and control of marine vehicles*.

[33] Thomas S Walton and Harry Polachek. Calculation of transient motion of submerged cables. *Mathematics of computation*, 14(69):27–46, 1960.

[34] Xiangqian Zhu and Wan Suk Yoo. Suggested new element reference frame for dynamic analysis of marine cables. *Nonlinear Dynamics*, 87(1):489–501, 2017.

Appendices

Appendix A

Parameters

Table A.1: Vehicle parameters

Parameter	Description	Units	Pro. Sph.	Myr. Pro.	Final SATLP
x_{n_2}	Bow end of nose section	m	0.4158	0.4158	0.4158
x_{n_1}	Aft end of nose section	m	-	0.2634	-
x_{m_2}	Bow end of mid section	m	-	0.2634	-
x_{m_1}	Aft end of mid section	m	-	-0.2070	-
x_{t_2}	Bow end of tail section	m	-	-0.2070	-
x_{f_2}	Bow end of fin section	m	-0.3130	-0.3125	0.3740
x_{f_1}	Aft end of fin section	m	-0.3740	-0.3745	0.3130
x_{t_1}	Aft end of nose section	m	-0.4158	-0.4158	-0.4158
l_v	Vehicle length	m	0.8316	0.8316	0.8316
d_v	Vehicle diamter	m	0.1238	0.1238	0.1238
h_f	Fin height	m	0.1096	0.1058	0.1270
m_v	Vehicle dry mass	kg	6.6094	6.6094	8.4335
∇	Displacement	m^3	0.0067	0.0081	0.0084
J_z	Moment of inertia	$kg \cdot m^2$	0.3872	0.3872	0.4605
a	length of nose section	m	-	0.1524	-
b	length of mid section	m	-	0.4704	-
c	length of tail section	m	-	0.2088	-
n	Exponential Myring Parameter	NA	-	2.0000	-
θ	Included tail angle	rad	-	0.4360	-

Table A.2: Fin parameters

Parameter	Description	Units	Prolate Spheroid	Myring Profile	SATLP
b_1	Trailing edge span	m	0.0825	0.0871	0.0843
b_2	Leading edge span	m	0.0688	0.0630	0.0660
b	Span	m	0.0756	0.0751	0.0752
c	Chord	m	0.0610	0.0620	0.0610
A_f	Fin area	m^2	0.0046	0.0046	0.0046
x_{f_1}	Fin trailing edge axial position	m	-0.3740	-0.3745	-0.3740
x_f	Fin centroid axial position	m	-0.3435	-0.3435	-0.3435
x_{f_2}	Fin leading edge axial position	m	-0.3130	-0.3125	-0.3131
AR_e	Effective aspect ratio	NA	2.5022	2.4389	2.4419
$C_{l\alpha}$	Lift Coefficient	NA	3.2889	3.2536	3.2537

Table A.3: Rope Parameters

Parameter	Description	Value	Units
M_r	Total Mass of the rope	16.2170	kg
L_r	Total length of rope	50.0000	m
r_l	Rope radius	0.0120	m
C_v	Viscous Damping Coefficient	250.0000	kg/s
E	Young's Modulus	2.08E-06	$kg/(m \cdot s^2)$
ρ_l	Rope Density	716.9489	kg/m^3

Appendix B

Final SATLP Vehicle Coefficients

Table B.1: Final nose-finned SATLP vehicle coefficients

Coef.	Units	Value	Coef.	Units	Value	Coef.	Units	Value
$X_{\dot{u}_b}$	kg	-0.4400	$Y_{\dot{r}_b}$	$kg \cdot m/rad$	0.3831	$N_{\dot{r}_b}$	$kg \cdot m^2/rad$	-0.3771
$X_{\dot{u}_f}$	kg	-0.0205	$Y_{\dot{r}_f}$	$kg \cdot m/rad$	-0.0610	$N_{\dot{r}_f}$	$kg \cdot m^2/rad$	-0.0184
$X_{\dot{u}}$	kg	-0.4465	$Y_{\dot{r}}$	$kg \cdot m/rad$	0.3221	$N_{\dot{r}}$	$kg \cdot m^2/rad$	-0.3955
$X_{\|u\|u_b}$	kg/m	-0.8573	$Y_{\|r\|r_b}$	$kg \cdot m/rad^2$	0.4970	$N_{\|r\|r_b}$	$kg \cdot m^2/rad^2$	-0.8421
$X_{\|u\|u_f}$	kg/m	-0.2311	$Y_{\|r\|r_f}$	$kg \cdot m/rad^2$	-0.3631	$N_{\|r\|r_f}$	$kg \cdot m^2/rad^2$	-0.1345
$X_{\|u\|u}$	kg/m	-1.0884	$Y_{\|r\|r}$	$kg \cdot m/rad^2$	0.1339	$N_{\|r\|r}$	$kg \cdot m^2/rad^2$	-0.9766
-	-	-	Y_{ur_b}	kg/rad	4.1812	N_{ur_b}	$kg \cdot m/rad$	-3.1778
-	-	-	Y_{ur_f}	kg/rad	-4.6043	N_{ur_f}	$kg \cdot m/rad$	-1.6262
-	-	-	Y_{ur}	kg/rad	-0.4231	N_{ur}	$kg \cdot m/rad$	-4.8040
-	-	-	$Y_{uu\delta_{rb}}$	$kg/(m \cdot rad)$	0.0000	$N_{uu\delta_{rb}}$	kg/rad	0.0000
-	-	-	$Y_{uu\delta_{rf}}$	$kg/(m \cdot rad)$	15.2931	$N_{uu\delta_{rf}}$	kg/rad	5.2532
-	-	-	$Y_{uu\delta_r}$	$kg/(m \cdot rad)$	15.2931	$N_{uu\delta_r}$	kg/rad	5.2532
-	-	-	Y_{uv_b}	kg/m	-20.5304	N_{uv_b}	kg	7.8247
-	-	-	Y_{uv_f}	kg/m	-17.3611	N_{uv_f}	kg	-6.0652
-	-	-	Y_{uv}	kg/m	-37.8915	N_{uv}	kg	1.7595
-	-	-	$Y_{\|v\|v_b}$	kg/m	-48.9083	$N_{\|v\|v_b}$	kg	0.4999
-	-	-	$Y_{\|v\|v_f}$	kg/m	-5.5540	$N_{\|v\|v_f}$	kg	-1.9103
-	-	-	$Y_{\|v\|v}$	kg/m	-54.4624	$N_{\|v\|v}$	kg	-1.4104
-	-	-	$Y_{\dot{v}_b}$	kg	-8.4726	-	-	-
-	-	-	$Y_{\dot{v}_f}$	kg	-0.1668	-	-	-
-	-	-	$Y_{\dot{v}}$	kg	-8.6394	-	-	-